Diplomarbeit

Epitaxial Growth of Quantum Dots by Successive Ionic Layer Adsorption and Reaction

Stefan Kraus

4. Oktober 2013

Johannes Gutenberg-Universität Mainz

durchgeführt am

Max–Planck–Institut für Polymerforschung
Max Planck Institute for Polymer Research

Betreuer: Prof. Dr. Mischa Bonn
Dr. Enrique Cánovas

Contents

1. Introduction

1.1. Motivation

Manufacturing cheap and efficient optoelectronic devices is a focus of research in electrical engineering, physics, chemistry and material sciences. Historically reducing cost has evolved from bulk, to thin film and recently to ultra thin film technologies. Very lately nanomaterials were applied to further reduce the amount of material needed for a working optoelectronic device. Cost reduction is not only achieved by reducing the amount of material consumed during production. In addition using low temperature processes and abundant materials is an important factor, too. A beautiful example of this trend is the history of solar cells. Starting from expensive bulk doped silicon solar cells, now cheap dye sensitized solar cells, mainly fabricated at room temperature from abundant low cost material have reached 14.1 % efficiency.[1] The latest step in the development of solar cells are quantum dot sensitized solar cells. Due to the quantum confinement in quantum dots the optical properties can easily be changed. Hence the light absorption can be predictably influenced. Figure 1 shows a set of quantum dot sensitized solar cells with different color stemming from different size quantum dots. Those new quantum dot sensitized solar cells reach an efficiency of 5.3 %.[2]

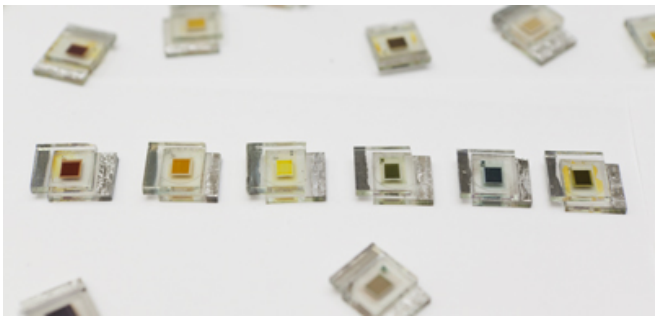

Figure 1.: Quantum dot sensitized solar cells with different quantum dot sizes.[3]

In additon quantum dots can be used to emit light, when a bias voltage is applied. As result quantum dots are nowadays incorporated in light emitting diodes as active material. Here the emitted wavelength is again a function of the quantum dot size. This is logical as absorption and emission properties are related to each other.

For both presented applications quantum dots are a good choice. Several general advantages of them, for example their large molar absorption coefficient or their bandgap tunability by size make them ideal building blocks for novel optoelectronic devices.

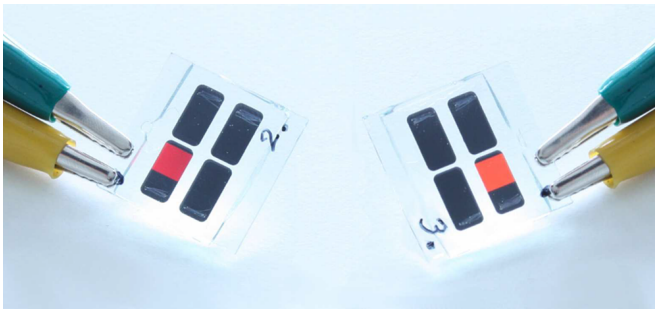

Figure 2.: Light emitting diodes with quantum dots as light emitters [4]

For quantum dots, two important subtypes in terms of cost an morphology are differentiated. The aforementioned cheaper colloidal quantum dots, for a schematic sketch see Figure 3a, are usually made at low temperature, covered by some sort of organic stabilizing agent and are soluble. The other subtype are epitaxial quantum dots, see Figure 3b for a schematic sketch, obtained from expensive high temperature processes *in vacuo*. Epitaxial quantum dots are grown directly on top of a solid substrate and lack the shell of a stabilizing agent. They are therefore insoluble.

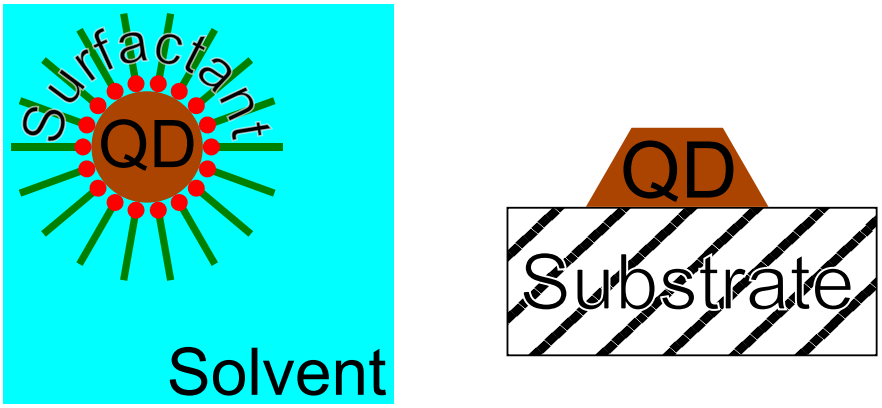

(a) Colloidal quantum dot, from cheap low temperature chemical synthesis

(b) Epitaxial quantum dot, from expensive high temperature growth

Figure 3.

In this work the focus is on the characterization of low cost, low temperature epitaxial quantum dots. Currently epitaxial quantum dots are routinely grown by a number of *established costly epitaxial methods*, mostly Molecular Beam Epitaxy (MBE) and Metal Organic Chemical Vapor Deposition (MOCVD). Their principles and underlying growth mechanisms will be discussed later in section 1.3, page 6.

Here the potential of growing quantum dots directly on a solid surface with successive ionic layer adsorption and reaction (SILAR) is studied. SILAR is a low cost room temperature procedure that was developed for thin films. Recently SILAR was employed for the synthesis of quantum dots on mesoporous oxide thin films. This work aims to replicate expensive MBE quantum dot growth by using the low cost SILAR technique.

A review of the work on SILAR for depositing thin films is available from Pathan *et al.*[5] The fundamentals of SILAR will be discussed in section 1.4, page 9.

1.2. What is a Quantum Dot (QD)?

A quantum dot is a nanoscopic structure of a certain semiconductor which has physical properties deviating from the bulk properties of that material. The most notorious being the possibility to tune the optoelectronic properties of the quantum dot by changing its size and shape, e.g. modifying the quantum confinement. In the bottom row of Figure 4 the transition of the density of states from a bulk to a quantum dot is depicted. In the left hand pane the density of states for a free electron in a semiconductor crystal is shown, a continuum of states with different energy is accessible by the electron. This represents the situation in a bulk material. In the middle pane the electron is confined in a thin film, in semiconductor context this is often referred to be a *quantum well*. The electron is confined in one dimension, it can move freely in the other two dimensions. This results in splitting the continuum of states into discrete energy levels. In the right hand pane the electron now is confined in all three dimensions. This so called quantum dot is termed to be zero dimensional, because the electron can not freely move into any direction and its characteristic energy band diagram is quantized. When going from 2D to 3D confinement, from a rod to a dot, at first there will be a small gap where there is for a given energy no state available. By further decreasing the size this gap in the density of states will grow bigger until it reaches a maximum width: then there is only an atom left. When this occurs the gap in the density of states will be the gap in energy between the highest occupied and the lowest unoccupied atomic orbital. Therefore one can tune this so called bandgap by simply changing the quantum dot size.

1.3. What is the Epitaxial Growth of Quantum Dots?

The two methods molecular beam epitaxy (MBE) and metal organic chemical vapor deposition (MOCVD) are typically used to deposit quantum dots (QD) onto a single crystal substrate. Usually MBE employs high vacuum conditions of 10^{-8} Pa and temperatures above 500 °C.[6] Molecular beam epitaxy setups are complex, an example setup is shown in Figure 5.

In MOCVD the substrate is also heated, but pressure ranges from reduced to standard pressure (2 kPa to 100 kPa). MBE growth rates are typically below 0.28 nm/s. A QD area density of $10^{11}/\mathrm{cm}^2$ is achievable.[8, p. 21] Also the amount of coverage to

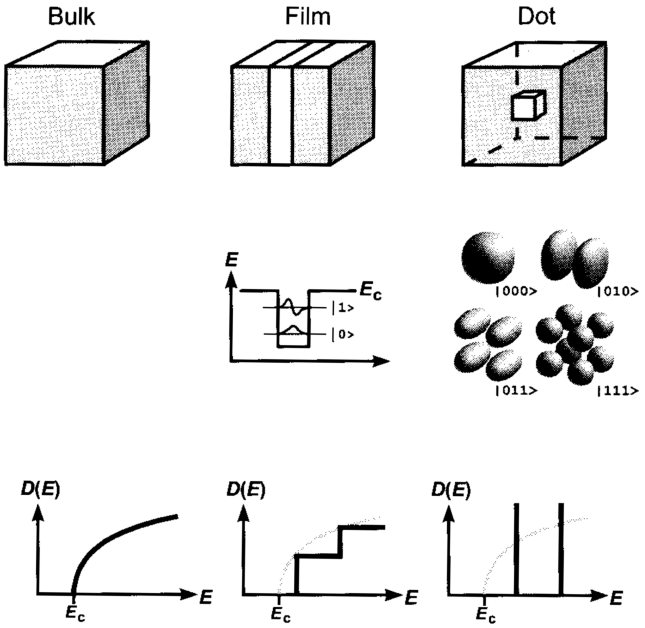

Figure 4.: Nature of electronic states in bulk material, quantum wells, and quantum dots. Top row: schematic morphology, center row: quantized electronic states, bottom row: density of states

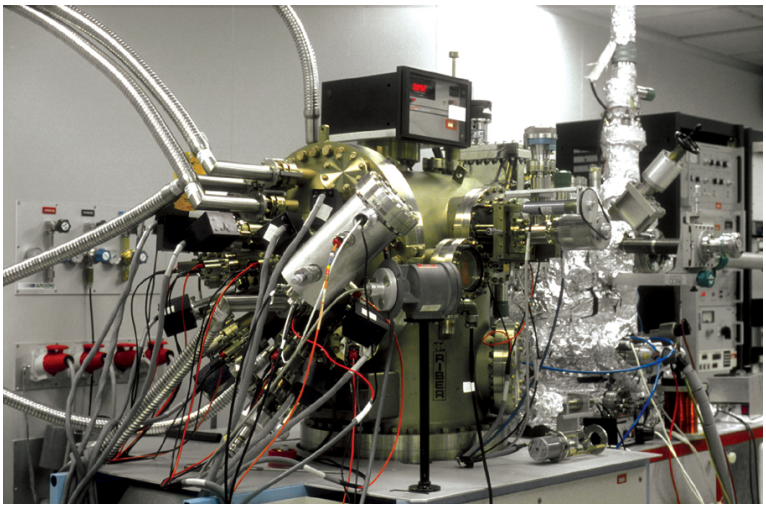

Figure 5.: Molecular beam epitaxy setup [7]

start island formation is a function of the lattice mismatch[9] ϵ; see Equation 1.

$$\epsilon = (d_2 - d_1)/d_1 \tag{1}$$

Whereas d_1 is the lattice constant of the substrate and d_2 is the lattice constant of the compound grown on top. To start island formation 4.2 monolayers of Ge are needed on Si.[10] When island nucleation starts, up to 90 % of the Ge in the islands can be provided by the wetting layer.[11] The work of Daruka and Barabási suggests that for any method that is capable of depositing material monolayer by monolayer, island formation can be expected under two conditions:[9] There needs to be a lattice mismatch ϵ between the substrate and the deposited material. Furthermore the system needs to be in thermodynamical equilibrium during deposition. For

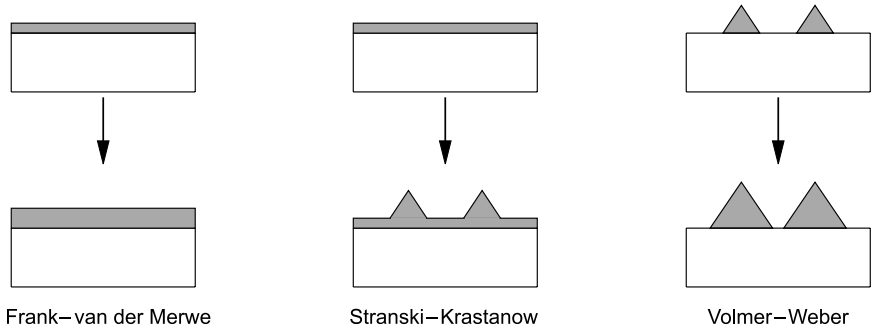

(a) Lattice match (b) Mild lattice mismatch (c) Strong lattice mismatch

Figure 6.: Different growth models in epitaxy [12, p. 8]

the classical epitaxial methods three growth mechanisms are usually discussed. For lattice matched materials *Frank-van der Merwe* growth (Figure 6a) is assumed. No difference in the lattice constants lets consecutive layers of material grow perfectly on top of each other and a film is grown. No quantum dots can be obtained. For mild lattice mismatch *Stranski-Krastanow* growth (Figure 6b) is assumed. After a first deposition of a thin film, called *wetting layer*, island nucleation starts when further layers are deposited. Semiconductor quantum dots will sit on a thin semiconductor film. In *Volmer-Weber* growth (Figure 6c) a strong lattice mismatch leads to immediate island formation. Quantum dots will reside directly on the substrate. These mechanisms can be compared to the surface tensions of liquids. Depending on the surface tension it is sometimes more favorable to form a droplet of liquid or to form a thin "wetting layer" on a substrate. The bigger the surface tension or the strain induced due to lattice mismatch, the earlier droplets, or islands, form. According to Daruka *et al.* island formation can be expected for any thermodynamically equilibrated deposition as long as a material dependent critical value for the lattice mismatch is reached.[9] They derived a theoretically model for a general phase diagram, this is shown in Figure 7.

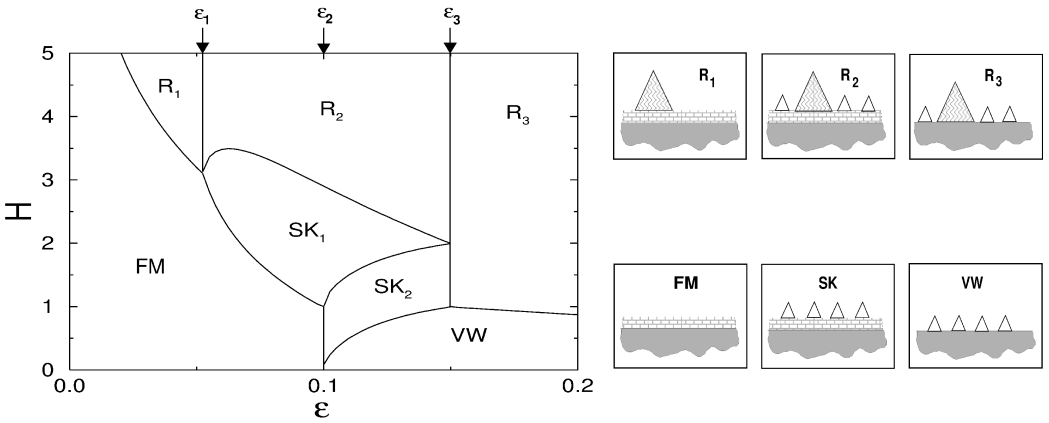

Figure 7.: Calculated phase diagram as a function of number of deposited monolayers H and lattice mismatch ϵ. Shaded triangles are ripened, empty triangles are stable islands. FM: Frank-van der Merwe, SK: Stranski-Krastanow, VW: Volmer-Weber, R: Phase with ripening. [9]

1.4. Successive Ionic Layer Adsorption and Reaction

In Successive Ionic Layer Adsorption and Reaction (SILAR) material is deposited layer by layer onto a substrate. The deposition of one layer is often referred to as *one SILAR cycle*. Figure 8 depicts the experimental procedure of one SILAR cycle to form one layer of compound AB. First, the substrate is immersed into a solution containing cations of sort A^+, those will adsorb onto the surface of the substrate and form an ionic layer on top of it. Second, the substrate, loaded with A^+, is immersed into clean solvent to rinse off any excess of A^+ which is not strongly bound to the substrate. After this rinsing step, an immersion of the substrate into a solution containing anions of sort B^- follows. Again ions will adsorb, to the currently A^+ rich surface, forming a layer of B^- ions. As a fourth step, excess B^- is rinsed away by immersing the substrate into clean solvent. Now the whole substrate should be coated with a layer of AB. Repeating this procedure increasing the number of cycles will lead to the layer-wise growth of an AB film. SILAR was introduced in the 1980s to form films of 300 nm thickness by Nicolau.[13] A SILAR synthesis can only be successful if AB is less soluble in the solvent than the two salts that are providing the ions A^+ and B^-. Otherwise the product of $A^+ + B^- \longrightarrow$ AB would be dissolved during the rinsing steps of each SILAR cycle.

Based on a review from Pathan and Lokhande Table 1 holds a list of selected substrate-coating combinations that have been investigated, mostly for thin films.[5]

For many coating substrate combinations the SILAR grown films are polycrystalline, as Figure 9a shows for PbS grown on a microscopy glass slide. An overview of film characteristics is available in the review paper [5] from Pathan and Lokhande. Recently SILAR has been employed to fabricate quantum dot sensitized solar cells. For those solar cells, SILAR is not performed on flat substrates but on mesoporous films of

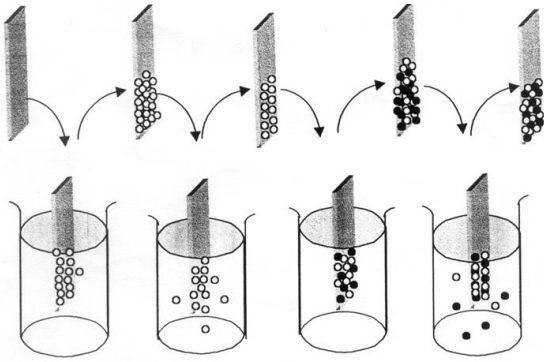

Figure 8.: SILAR principle [5]

Table 1.: List of selected SILAR substrate-coating systems [5]

On glass Substrate:						
CuS	ZnS	CdS	In_2S_3	PbS	CdSe	CdTe
On indium doped tin oxide substrate:						
CuS	ZnS	CdS				
On fluorine doped tin oxide:						
CdSe						
On silicon (111):						
CuS	PbS					

several µm height.[15] Only a few SILAR cycles are carried out during which quantum dots are deposited into the mesoporous film. For cadmium selenide quantum dots on mesoporous titanium dioxide a cycle dependent change in light adsorption can be observed with the eye. As Figure 9b shows, their color changes from green-yellow after one SILAR cycle, over orange after three and four SILAR cycles to dark red after six cycles of SILAR. Similar results have been reported for other compounds.[16]

Even though SILAR is used to synthesize epitaxial quantum dots for sensitized solar cells, up to now, no systematic studies of the quantum dot growth have been carried out. Usually growing conditions are established by trial and error, often solely optimizing for high light to electric power conversion efficiency. This Diplomarbeit was undertaken to give an insight into the growth mechanism of SILAR fabricated quantum dots and to employ this fundamental knowledge for controlling quantum dot properties and their spatial distribution.

As a model system SILAR grown PbS on flat TiO_2 rutile single crystals was chosen. PbS is already established in sensitized solar cells where mesoporous TiO_2 acts as substrate.[17] To simplify the system the (100) face of TiO_2 rutile was selected as

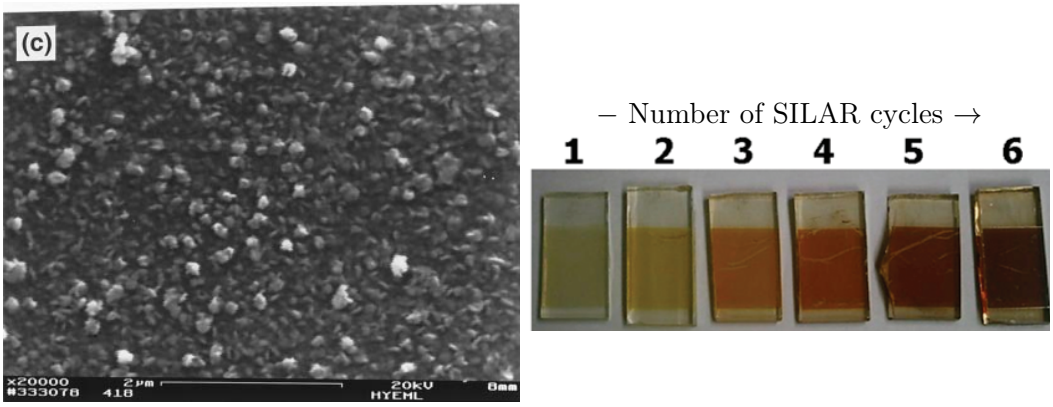

(a) SEM micrograph of polycrystalline PbS film from SILAR on glass [14]

(b) Substrates for CdSe quantum dot sensitized solar cells, after different number of SILAR cycles [15]

Figure 9.: Examples of SILAR

substrate. The surface is oxygen terminated and should therefore easily adsorb Pb^+ ions in the first step of a SILAR process.[18]

During successive ionic layer adsorption and reaction many experimental conditions can be varied. At least two different precursor solutions are in involved. Each of them can have its own concentration. The solvent for the precursors can differ. Considering the Langmuir model of adsorption,[19] shown in Equation 2, where K is the equilibrium constant, θ is the fraction of the surface covered by the adsorbate and c is the concentration of adsorbate in the solution,

$$K = \frac{\theta}{(1-\theta)c} \tag{2}$$

one can conclude that the coverage of the substrate during immersion into a SILAR precursor bath is a function of the adsorbate concentration, as this formula can be rearranged into Equation 3.

$$\theta = \frac{Kc}{1+Kc} \tag{3}$$

Furthermore, as SILAR is an equilibrium method, the van 't Hoff equation, Equation 4 is obeyed.[20, pp. 236, 991]

$$\left(\frac{\partial \ln K}{\partial T}\right) = \frac{\Delta_{\mathrm{ad}} H^{\ominus}}{RT^2} \tag{4}$$

Here T is the temperature, R the gas constant and $\Delta_{\mathrm{ad}} H^{\ominus}$ the standard enthalpy of adsorption. A result of this is that when temperature is changed the equilibrium constant K will also change. A change in K, on the other hand, will lead to a change in coverage θ. Thus bath temperature should also have an influence onto the growth

of quantum dots from SILAR as the amount of material deposited per SILAR cycle can be varied.

As a starting point precursor concentrations of 0.02 mol/L $PbNO_3$ and anhydrous Na_2S, both in Methanol, were used. Those were already used in experiments with PbS quantum dot sensitized solar cells.[21]

2. Epitaxial Growth of Quantum Dots by SILAR

2.1. Effects of Inert and Oxidative Atmosphere

As a first step it was tested if the experiments needed to be carried out in inert atmosphere. Lead sulfide is known to adsorb oxygen and to transform its surface to lead oxide at room temperature.[22] This is obvious when the standard Gibbs energy of the reaction of lead sulfide to lead oxide, presented in Equation 5, is calculated following Hess's law.

$$\mathrm{PbS} + 1.5\,\mathrm{O_2} \longrightarrow \mathrm{PbO} + \mathrm{SO_2}\uparrow \tag{5}$$

$$\Delta_r G^{\ominus} = \sum \Delta_\mathrm{f} G^{\ominus}_{products} - \sum \Delta_\mathrm{f} G^{\ominus}_{reactants} \tag{6}$$

For lead sulfide the standard Gibbs energy of formation is $\Delta_\mathrm{f} G^{\ominus} = -98.7\,\mathrm{kJ/mol}$ and for lead oxide the standard Gibbs energy of formation is $\Delta_\mathrm{f} G^{\ominus} = -188.9\,\mathrm{kJ/mol}$. Sulfur dioxide has a standard Gibbs energy of formation of $\Delta_\mathrm{f} G^{\ominus} = -300.1\,\mathrm{kJ/mol}$ and the value for elemental oxygen is $\Delta_\mathrm{f} G^{\ominus} = 0\,\mathrm{kJ/mol}$ by definition.[23] Therefore the standard Gibbs energy of the reaction is $\Delta_r G^{\ominus} = -390.3\,\mathrm{kJ/mol}$ and thus favorable.

As this does not tell anything about the reaction rate, one might argue that its effect is negligible if the rate is slow enough to convert only a very small fraction of the lead sulfide surface into lead oxide in between the SILAR cycles. An oxide layer forming after each SILAR cycle would introduce an unwanted layer of complexity as the next cycle would neither be grown on lead sulfide nor on titanium dioxide. With such a growth mechanism similarities to epitaxial growth methods, presented in section 1.3 (see from page 6), are not expected and therefore quantum dot formation would be unlikely.

To test this hypothesis the (100) faces of different titanium dioxide rutile single crystals were subject to lead sulfide SILAR processes with one and five cycles in inert nitrogen atmosphere and in air. For the samples prepared under inert atmosphere the procedure given in appendix A.1, page 53, was followed omitting the wetting and final methanol rinse III steps. For the oxidative atmosphere samples wetting and final methanol rinse III were also omitted. In addition the solutions and solvents were never deoxygenated and the SILAR process was not carried out in a glove box but in an ordinary fume hood. For the sample consisting of one cycle SILAR under oxidative atmosphere the sodium sulfide concentration was 0.06 mol/L, all other concentrations were according to the method given. An overview of the experimental conditions is given in Table 2. Atomic force microscopy images of the samples were taken either on

Table 2.: SILAR conditions for inert and oxidative atmosphere experiments

Step	No. of cycles	Immersion time / s	Concentration
Wetting		no immersion	
Pb^{2+}	1, 5	20	$0.02\,\mathrm{mol/L} = c_0$
Rinse I	1, 5	30	
S^{2-}	1, 5	20	$0.02\,\mathrm{mol/L} = c_0$ *
Rinse II	1, 5	20	
Rinse III		no immersion	

*: for the 1 cycle in air sample $0.06\,\mathrm{mol/L} = c_0$ Na_2S in methanol

the same day after the SILAR process or up to one week later and are presented in Figure 10.

After one cycle there is no visible difference between the sample prepared in oxidative atmosphere (Figure 10a) and in inert atmosphere (Figure 10b). Both samples show a fine grained background with grains of the same height. From the background dozens of laterally larger grains stand out, exceeding 5 nm in height.

Comparing the samples with five SILAR cycles to each other gives a different picture. The sample with five cycles in air Figure 10c exhibits a relatively smooth surface composed from many smaller grains. The five cycles sample prepared in inert atmosphere Figure 10d clearly has different characteristics. Although being made up from distinct grains, those are larger in lateral scale and exceed a height of 5 nm more often.

The similar results after one cycle SILAR are not surprising. As there is only one layer of lead sulfide coating, whilst no further SILAR cycles are applied, surface oxidation will not induce any effect on the resulting topography. In air, the surface might get oxidized immediately after the SILAR process or even while it is still immersed into the precursor solution. In inert atmosphere, oxidation is prevented during SILAR, but the surface will eventually get oxidized when the sample is retrieved from the glove box and atomic force microscopy is carried out in air. Therefore the net result is identical; one layer of lead sulfide with a lead oxide surface.

The sample consisting of five cycles SILAR performed in air shown in Figure 10c is very similar in terms of topography to both samples consisting of one cycle SILAR, either performed in air (Figure 10a) or in inert atmosphere (Figure 10b). When the SILAR process was carried out under oxidative atmosphere the topography did not change any more after the first cycle SILAR.

The sample with 5 cycles SILAR prepared under inert atmospheres (Figure 10d) shows a change in topographic features after the first cycle SILAR.

As the presented topographic data depends on the oxidative conditions the following two growth mechanism may be discussed for the evolution of topographic features under the conditions of the SILAR process used. First, under inert conditions growth during SILAR cycles two to five prefers to increase the size of some already existing grains

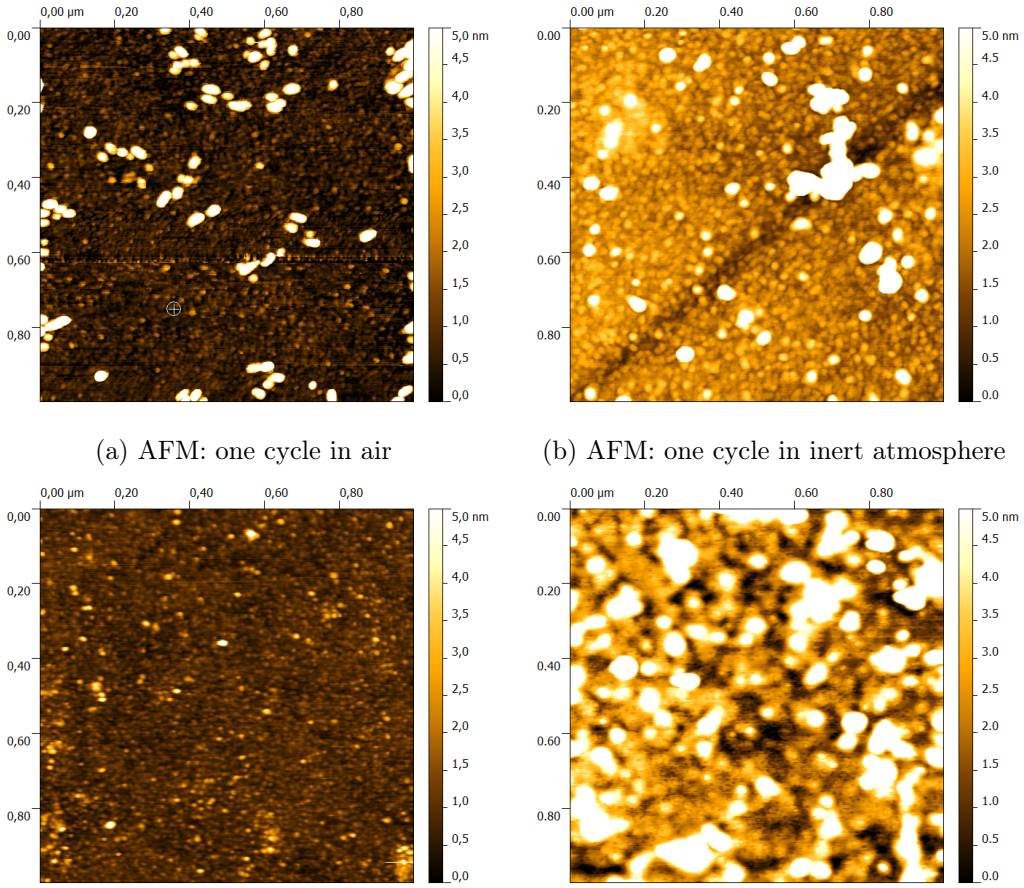

(a) AFM: one cycle in air

(b) AFM: one cycle in inert atmosphere

(c) AFM: five cycles in air

(d) AFM: five cycles in inert atmosphere

Figure 10.: Topography after different number of PbS SILAR cycles in air and in inert atmosphere

and yields particles with different sizes. Second, under oxidative conditions growth during SILAR cycles two to five seems to mimics the nucleation of grains during the first cycle SILAR yielding uniform looking particles.

To influence the size of quantum dots one should therefore perform the presented SILAR experiments under inert atmosphere. SILAR experiments performed in oxidative atmosphere might result in less or no influence on the size of quantum dots or nanoparticles.

Conclusions about Effects of Inert and Oxidative Atmosphere *At least for the methanolic lead sulfide SILAR process using the conditions presented here it seems mandatory to work in an oxygen free environment. It might be worth to consider if speeding up the transfer between immersion baths could allow for processing in oxidative atmosphere. A layer of adhering solvent might protect the lead sulfide quantum dots*

from oxidizing during a rapid transfer. On the other hand oxygen will still be present dissolved in the solutions. SILAR deposited materials other than lead sulfide should also be studied to see if they are also prone to oxidation during SILAR. The review from Pathan et al. *can give some suggestions, or Table 1, which holds a selected list from that review.[5]*

2.2. Cycle Dependence

In quantum dot sensitized solar cells the number of SILAR cycles is often used to control the size of quantum dots and thus the light absorption properties of the solar cell, as already discussed in section 1.4 on page 9. It is therefore important to follow the evolution of quantum dots in the model system lead sulfide on titanium dioxide rutile (100) face over an increasing number of SILAR cycles.

For cubic crystalline lead sulfide it is known that the (111) plane consists only of lead atoms and the (222) plane only of sulfur atoms.[24] During one SILAR cycle an already existing lead sulfide crystal should grow epitaxially into the [222] direction. For a cubic crystal one can calculate the inter lattice plane distance $d_{(hkl)}$ from the lattice constant a and the miller indices h, k, l according to Equation 7.[25, p. 221]

$$d_{(hkl)} = \frac{a}{\sqrt{h^2 + k^2 + l^2}} \tag{7}$$

With $h = k = l = 1$ and $a = 5.935 \times 10^{-10}\,\mathrm{m}$, from reference [26], one can calculate the distance between two planes of lead to be $d_{(111)} = 3.42 \times 10^{-10}\,\mathrm{m}$. This is the theoretical ingrowth of a lead sulfide crystal's thickness during one cycle of SILAR, if only one side is coated with PbS. The distance between a lead and sulfur plane on the other hand is $d_{(222)}$, in the cubic crystal system this can be written as half of $d_{(111)}$, Equation 8. The calculated value is $d_{(222)} = 1.71 \times 10^{-10}\,\mathrm{m}$.

$$d_{(222)} = \frac{1}{2} d_{(111)} \tag{8}$$

Now let Δz_1 the thickness ingrowth during the first cycle of SILAR, on a hypothetical mathematical perfect flat plane, be modeled as the sum of: $r_{S^{2-}}$ the ionic radius of S^{2-}, which acts as spacer between the flat plane and the lattice planes in the PbS crystal; $d_{(222)}$ the inter lattice plane distance between sulfur and lead; and $r_{Pb^{2+}}$, which acts as spacer against the environment. Equation 9 shows this sum.

$$\Delta z_1 = r_{S^{2-}} + d_{(222)} + r_{Pb^{2+}} \tag{9}$$

Any further SILAR cycle will add another $d_{(111)}$ to Δz_1. Using Equation 8 and introducing the variable number of SILAR cycles n, the thickness ingrowth can be predicted to be

$$\Delta z_n = r_{S^{2-}} + (2n - 1) \times d_{(222)} + r_{Pb^{2+}} \tag{10}$$

With $r_{S^{2-}} = 1.84 \times 10^{-10}\,\mathrm{m}$ and $r_{Pb^{2+}} = 1.19 \times 10^{-10}\,\mathrm{m}$ obtained from reference [23] calculations can be carried out.

To check for the presented cycle dependent properties the general procedure for SILAR found in appendix A.1, page 53, was applied to three specimens of titanium dioxide rutile single crystals with polished (100) faces. The experimental conditions are tabulated in Table 3. The samples were subject to one, three and five cycles of SILAR.

Table 3.: SILAR conditions for cycle dependence experiments

Step	No. of cycles	Immersion time / s	Concentration
Wetting		30*	
Pb^{2+}	1, 3, 5	20	$0.02\,\mathrm{mol/L} = c_0$
Rinse I	1, 3, 5	30	
S^{2-}	1, 3, 5	20	$0.02\,\mathrm{mol/L} = c_0$
Rinse II	1, 3, 5	20	
Rinse III		70*	

* : 5 cycle sample was not subjected to wetting and rinse III

During the preparation of the five cycles sample wetting and the final methanol rinse III were skipped. Atomic force microscopy images of all samples were taken within one week after the respective SILAR process. In addition a pristine titanium dioxide single crystal was investigated with the atomic force microscope. Topographic AFM images are presented in Figure 11a for the pristine and in figures 11b, 11c, 11d for the one, three and five cycles samples respectively.

All atomic force microscope measurements and the data derived from them only contain relative height information. As described in appendix B.1.1, page 58, the lowest height within one atomic force microscope image is routinely set to be zero height. Therefore all data is evaluated under the assumption that the bare substrate has been measured in every atomic force microscope image taken in at least one pixel. With that assumption every other height measured is the height above the substrate. This assumption is believed to be true as long as the surface is not completely covered by grains or particles. For densely covered substrates the calculated height values are expected to be smaller than the real height above the substrate. For substrates sparsely covered by grains the measured heights also might differ from the real heights above the surface, as the bare substrate surface may have steps and other topographic feature of its own.

The pristine rutile crystal exhibits a homogeneously flat surface, with sub nanometer height deviation over one micrometer scan length. Though some imperfectnesses are present on the surface, in Figure 11a a grain with a height of 4 nm, measured from the lowest pixel in the image, is visible in top right part of the image. Another feature quite often present on the crystal surface are straight trenches only few nanometers in depth, several dozens of nanometers wide and many microns long. They seem to have no preferential orientation. They are probably a result of the cutting and polishing of the crystals. Figure 11a does not show a pronounced trench, but the one cycle sample

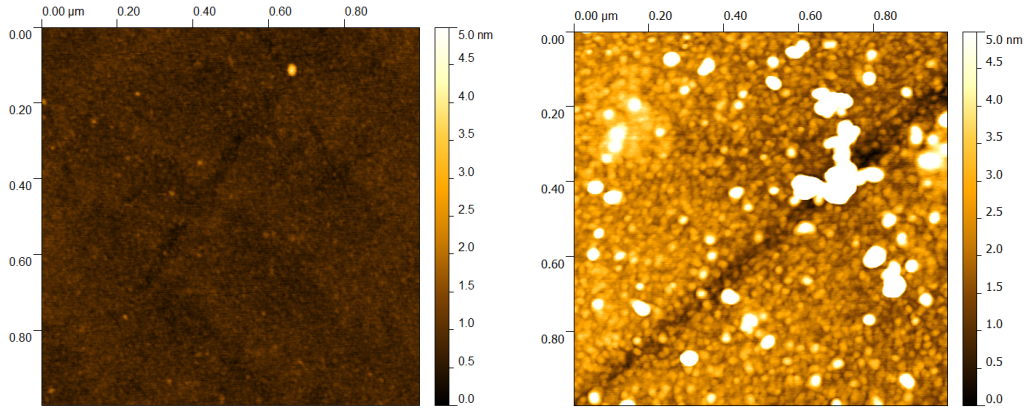

(a) AFM: pristine rutile sample

(b) AFM: one cycle of PbS SILAR

(c) AFM: three cycles of PbS SILAR

(d) AFM: five cycles of PbS SILAR

Figure 11.: Topography after different number of SILAR cycles. Same height scale bar from 0 nm to 5 nm was chosen to directly indicate the change in particle size by cutting through the plane of same height at 5 nm.

has an easy to spot trench running from bottom left to top right in Figure 11b.

After one cycle of SILAR the surface is covered completely with a rough layer of lead sulfide being made up from individual grains. There are some particles exceeding a height of 5 nm scattered on the surface.

Three cycles of SILAR, presented in Figure 11c, lead to surface morphologies related to one cycle SILAR. The surface is uniformly covered by individual but a bit larger grains. On this background layer many particles exceeding a height of 5 nm are found.

After five cycles of SILAR, distinct grains of various sizes and heights are visible in Figure 11d. It is difficult to tell a background layer apart from higher grains. Many of the particles higher than 5 nm seem to be conglomerates of what were separated particles after three and one cycle of SILAR. It resembles more the polycrystalline look of lead sulfide thin films prepared by Kanniainen *et al.* already presented in

Figure 9a, page 11.[14] In their studies on lead sulfide thin films Kanniainen *et al.* demonstrated that the thickness of lead sulfide thin films scales proportionally with the number of SILAR cycles.[14] Overall the samples presented in this section seem to rather mimic thin film growth in contrast to a sample resulting in isolated quantum dots which will be presented later in section 2.4, page 26.

Using the computer software `Gwyddion`, see appendix C.1 page 60 for details, the height distribution can be extracted from AFM data. The height distribution is a normalized plot of the probability density ρ. It gives a number with which fraction a certain height z is present in the analyzed AFM image. The area under the plot is normalized to equal unity. Height distributions were extracted from all four sets of AFM data presented in Figure 11. Equation 10 was used to calculate the predicted height ingrowth after 1, 3, and 5 cycles. To the numbers calculated the peak maximum of the pristine sample's height distribution was added each. This should account for a non-perfect epitaxial growth and the substrate's deviation from the assumption of a perfect flat surface used to derive Equation 10. The combined plot of the height distributions together with the predicted heights is depicted in Figure 12a. One should remember that the heights presented are relative heights using the lowest point in each atomic force microscope image as a zero reference, as it was discussed on page 17. The heights of the high number of SILAR cycles might be underestimated. However, note that the measured heights roughly follow a linear ingrowth which is expected for thin film growth of lead sulfide.[14] This roughly constant ingrowth of thickness per SILAR cycle provides a preliminary proof that nearly always the lowest point in the presented AFM images can be attributed to the bare substrate and that a polycrystalline thin film growth mechanism might take place. In addition only the general form of the height distribution and the position of its maximum will be discussed. As the samples analyzed in this section are lower in quality than the sample of isolated quantum dots which will be presented in section 2.4, page 26 the fast and easy to access shape of the height distribution and the also fast and easy to access maximum of the height distribution will be used as a rough indication of cycle dependent properties. For a better set of samples, which need to be prepared in the future following the procedure for the sample of isolated quantum dots (section 2.4, page 26) one should discuss their cycle dependent properties based on the different moments of the height distribution like the mean (first moment), variance (second moment), skewness (third moment) and kurtosis (fourth moment).

The pristine rutile sample shows a sharp maximum of the probability density at 0.7 nm. Heights above 1.5 nm are barely present and not a single pixel exceeds the height of 3.9 nm. This fulfills what is expected from a flat but not perfect surface.

After one cycle SILAR, the maximum of the height distribution is at 1.2 nm, coinciding with the predicted height ingrowth of 1.2 nm. In addition the peak broadens and begins to grow a tail towards greater height values. Heights above 4 nm are barely present, but pixels with a height greater than 8 nm are present. Many small grains with nearly the same height covering a flat surface will give such a distribution. This is in accordance with the features seen in Figure 11b.

Three cycles of SILAR give a broad height distribution peak with a long tail up to

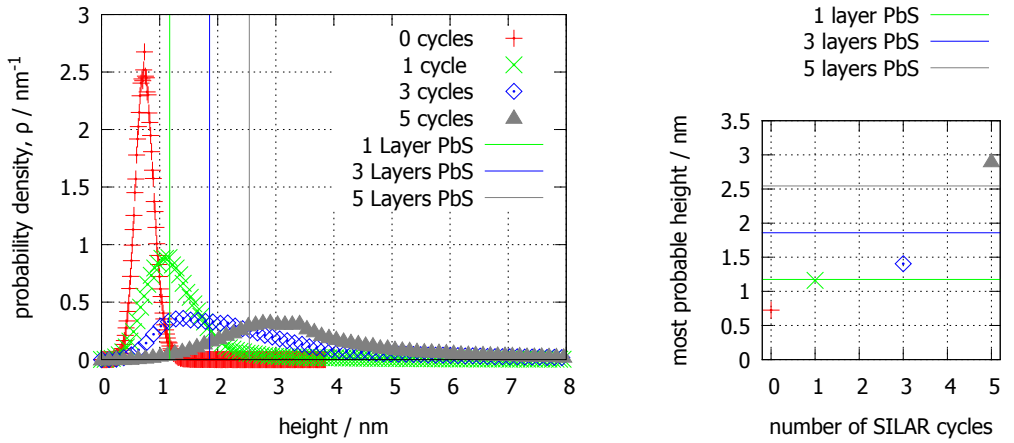

(a) Height distributions

(b) Most probable height

Figure 12.: Cycle dependent topographic properties. Horizontal and vertical lines are predicted height ingrowths.

5 nm. The maximum of the height distribution for three cycles SILAR is at 1.4 nm, not far from the one cycle's maximum. The height predicted for three cycles is 1.9 nm, which is not right at the maximum of the plot, but still part of the broad peak before its fast decline. On the other hand the probability density at the maximum for the three cycles sample is only of half the value after one cycle. The background of this image is made up of small, similar grains responsible for the first rise of the plot. The numerous particles with peak heights above 5 nm, which appear white in the AFM image Figure 11c, are responsible for the broadening and the long tail, as they are standing out from the background grains.

The height distribution of the five cycles SILAR sample has its highest value at 2.9 nm and is broad. Whereas a height ingrowth of 2.5 nm was predicted. The onset is not as steep as after three cycles of SILAR. The tail extends up to 7 nm before the probability density drops to nearly zero. With the slow rise at low heights, the five cycles samples have characteristics of a system put together from large inhomogeneous particles without a background layer made from smaller more homogeneous grains. The big particles seem to cover whatever is beneath them completely.

The height where the maximum of the probability density is located can be seen as the height value most probably to be found in an AFM data set. This most probable height is plotted against the number of SILAR cycles in Figure 12b, in addition the predicted height ingrowths caused by 1, 3 and 5 cycles SILAR are shown. The most probable height clearly increases with the number of SILAR cycles. This is in agreement with predictions and experiments for SILAR grown lead sulfide thin films.[14] On the other hand in section 2.4, page 26 a sample will be presented that does not fulfill the predictions on thin film growth but exhibits the nucleation of isolated lead sulfide quantum dots. From the figure presented it is intriguing to imply a linear relationship

between the number of cycles and the most probable height. A naive assumption is that SILAR, as a layer by layer method, adds the same amount of material during each cycle. Coating a flat surface, one might expect a linear ingrowth of some height property like the absolute average height, the height difference between highest and lowest point in a data set, the most probable height, or their like. The predicted height ingrowths plotted are based on that assumption. With only four data points the statistical reliability of linear fitting the most probable height to the number of cycles would be questionable and therefore was not done.

The tentatively suggested cycle dependence bears some complexity. It is not a single, chosen observable feature that changes with the number of SILAR cycles; like increasing the number of grains, or only the size of grains. Instead the morphology undergoes a transformation through several stages when the number of SILAR cycles is increased. Though the derived quantity of the most probable height seems to exhibit a correlation with the number of SILAR cycles applied. This might turn out as a linear relation, when further studies have been conducted.

From the plots in Figure 12, one can deduce that there is a cycle dependent change in topography. If the growth would be perfectly epitaxial all height distribution plots would look like the pristine sample, its surface would just be copied layer by layer. Even the position would not change as with the atomic force microscope, as set up, only relative heights can be measured. After one cycle of SILAR, island formation is already visible as the height distribution broadens and the most probable height increases. After this, the height distribution of the three cycles SILAR sample suggests that all particles grow, with some of them growing faster to give the high heights tail in the plot. The most probable height increases further, but is associated with a smaller step in height, even though the number of cycles is increased by two and not only by one. These results can be understood from the following scenario: The most probable height does not increase that much when only some preferred grains grow, as the majority stays smaller, with the same height. In the five cycles SILAR sample the growth of large individual particles from fusing several smaller grains together took place. The fusion into bigger and higher particles is already visible in the height distribution plot of the three cycle sample, as it shows characteristics of a bimodal distribution. One part being the large particles which are well developed after five cycles SILAR, the other part being small grains already residing on the surface after one cycle SILAR. The most probable height now makes a big leap upward as even the slowly growing grains reach a certain height and further more get merged into other grains by fusing with the fast growing grains.

The amount of material that is deposited onto a substrate during one cycle of SILAR is of great interest as this is the material that allows for the growth of quantum dots. Especially as cycle dependence experiments suggest that increasing the number of cycles very quickly leads to big quantum dots, it is important to check if decreasing the amount of material deposited per cycle is possible. If the precursor concentrations are reduced one reduces the amount of ions that can adsorb to the substrate's surface, see Equation 3, page 11, and therefore concentration decrease should have a similar influence as decreasing the flux in a molecular beam epitaxy.

Conclusions about Cycle Dependence *The size of synthesized nanocrystals can be controlled by changing the number of SILAR cycles. Their height scales, at least for the samples analyzed here, approximately with the predicted number of deposited lead sulfide layers. Large broadening of the height distributions with increasing number of SILAR cycles is characteristic for the growing conditions used here. For most applications narrow size distributions are desirable, so for defining distinct properties of quantum dots employing the here used method of methanolic lead sulfide SILAR should be limited to very few cycles. Further optimization of reaction condition, though, may narrow down the size distribution for the method used in this study. Metal complexing agents in the lead precursor solution for example can influence the height ingrowth per cycle.[27] The advantage of controlling the size with the number of cycle is the ease of implementation. In molecular beam epitaxy and the chemical vapor based methods large efforts need to be taken to control the flux of the different reactants, often at the same point of time. With its successive approach SILAR avoids the need for sophisticated flux control. The amount of material deposited per cycle is inherently limited. Again it needs to be stressed that the situation may be different for other substrate-coating combinations. If the quantum dot nucleation in the here presented system really mimics the Stranski-Krastanow growth, described in section 1.3, different compounds with different lattice mismatch will yield other results. This is in need of further investigation to extend the knowledge of how the different growth modes usually discussed for epitaxial methods, Frank-van der Merwe, Stranski-Krastanow, and Volmer-Weber, can be applied to quantum dot nucleation with SILAR. If those were applicable predictions about cycle dependent properties might be possible in the future for SILAR.*

2.3. Concentration Dependence

Material flux rates are the primary knob for controlling growth rates in molecular beam epitaxy and chemical vapor deposition. The analogy to material flux in successive ionic layer adsorption and reaction are the precursor concentrations. Material flux and precursor concentration should both influence the growth mechanism of a coating layer. A low flux or concentration is expected to be closer to equilibrium conditions as the local environment has time to settle into the thermodynamic minimum. High fluxes and concentrations should favor kinetic products by depositing material in shorter time scales than the needed equilibration time. In addition, desorption and dissolution play an important role at the interface of the liquid and solid phase in SILAR. This has been discussed in context with the Langmuir model in section 1.4.

To investigate to what extent the precursors' concentrations influence the nucleation during a SILAR process, a concentration series experiment was set up. On four titanium dioxide single crystals (100) face, a five cycle SILAR procedure following the instructions in appendix A.1 on page 53 was employed. The concentrations for the four samples were: $c_0 = 2 \times 10^{-2}\,\mathrm{mol/L}$, $c_1 = 2 \times 10^{-3}\,\mathrm{mol/L}$, $c_2 = 2 \times 10^{-4}\,\mathrm{mol/L}$, and $c_3 = 2 \times 10^{-5}\,\mathrm{mol/L}$. An overview of the experiments conditions is presented in Table 4. The resulting atomic force microscopy images are shown in Figure 13.

Table 4.: SILAR conditions for concentration dependence experiments

Step	No. of cycles	Immersion time / s	Concentrations
Wetting		30	
Pb^{2+}	5	20	2×10^{-2} mol/L $= c_0$, 2×10^{-3} mol/L $= c_1$, 2×10^{-4} mol/L $= c_2$, 2×10^{-5} mol/L $= c_3$
Rinse I	5	30	
S^{2-}	5	20	2×10^{-2} mol/L $= c_0$, 2×10^{-3} mol/L $= c_1$, 2×10^{-4} mol/L $= c_2$, 2×10^{-5} mol/L $= c_3$
Rinse II	5	20	
Rinse III		70	

Just from the visual appearance of the AFM images, the sample set can be divided into two subsets. The two higher concentration samples, c_0 and c_1 shown in Figure 13a and Figure 13b, have particles and grains covering the whole measured area. The second subset contains the two lower concentration samples c_2 and c_3 that are shown in Figure 13c and Figure 13d. These samples' surfaces are not wholly covered by grains or particles. There are well separated particles visible on a flat background. The background resembles the surface of pristine rutile which was already shown in Figure 11a on page 18 and described in context of cycle dependent properties in section 2.2. Within the two subsets of the concentration series the particle density, lateral size and height is different between the two samples each.

As previously done the height distributions were extracted from the AFM data sets and plotted in Figure 14a. The height distribution of a pristine titanium dioxide crystal surface was included additionally. The limitations and assumptions for this analysis were already described and discussed in section 2.2 on page 17.

Although again the shape of the height distribution represents a very rough estimate one can resolve two sets of results. The first set contains the two samples treated with the two low concentrated precursor solutions c_3, and c_2. Both of them mimic the height distribution of the pristine titanium dioxide rutile (100) surface. Therefore all three have a narrow height distribution peaking around 0.8 nm.

The two higher concentration samples, c_1 and c_0, have nearly identical height distributions both peaking at 2.9 nm. Their peaks are broad and their tails extend up to 7 nm.

The peak position of the probability density plot can be regarded as the most probable height within that sampled area. This most probable height is plotted against the used precursor solution in Figure 14b; the height most probable height from a pristine rutile crystal is shown as a horizontal red line.

In this plot the two subsets of the concentration experiment are clearly distinct. Both higher concentration samples yield the same most probable height. The two lower concentration samples give values scattered around the value of pristine rutile.

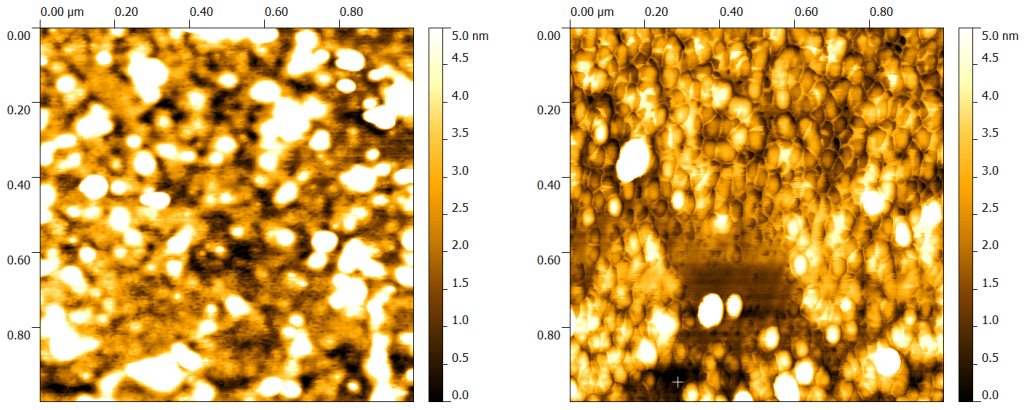

(a) AFM: $c_0 = 2 \times 10^{-2}\,\mathrm{mol/L}$

(b) AFM: $c_1 = 2 \times 10^{-3}\,\mathrm{mol/L}$

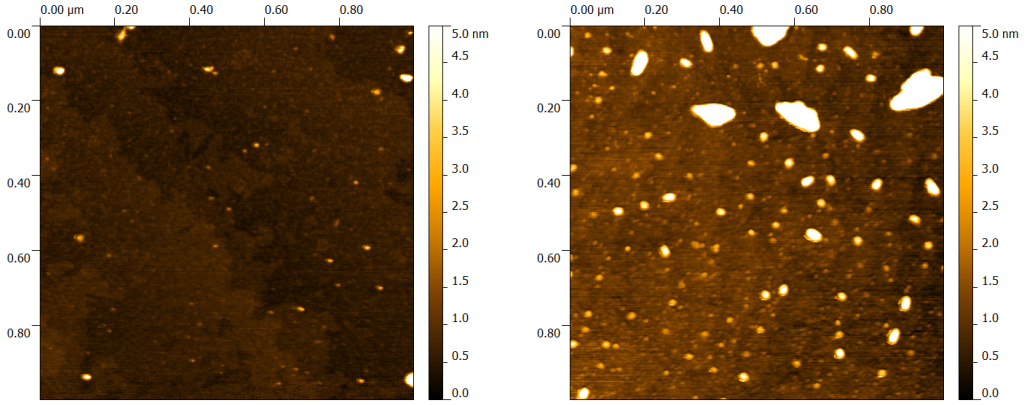

(c) AFM: $c_2 = 2 \times 10^{-4}\,\mathrm{mol/L}$

(d) AFM: $c_3 = 2 \times 10^{-5}\,\mathrm{mol/L}$

Figure 13.: Sample topography after five cycles SILAR with different precursor concentrations c_i

Within the limited tests performed these results lead to the conclusion that there is a threshold concentration below no significant material deposition takes place during the five SILAR cycles investigated in the concentration series. This threshold must lie between $c_2 = 2 \times 10^{-4}\,\mathrm{mol/L}$ and $c_3 = 2 \times 10^{-5}\,\mathrm{mol/L}$. Above this threshold, enough material is deposited to form a stable layer of lead sulfide which is not rinsed away during the various rinsing steps of a SILAR process.

Another observation is that both high concentration samples have nearly identical height distributions and share the same most probable height. After passing the minimal concentration threshold a further tenfold increase of the precursor concentrations apparently only has a weak effect on height distribution. From the figures of height distribution one might imply that with both different high concentrations $c_0 = 2 \times 10^{-2}\,\mathrm{mol/L}$ and $c_1 = 2 \times 10^{-3}\,\mathrm{mol/L}$ the same amount of material was deposited. This implication might be wrong, as the absolute thickness of the lead sulfide

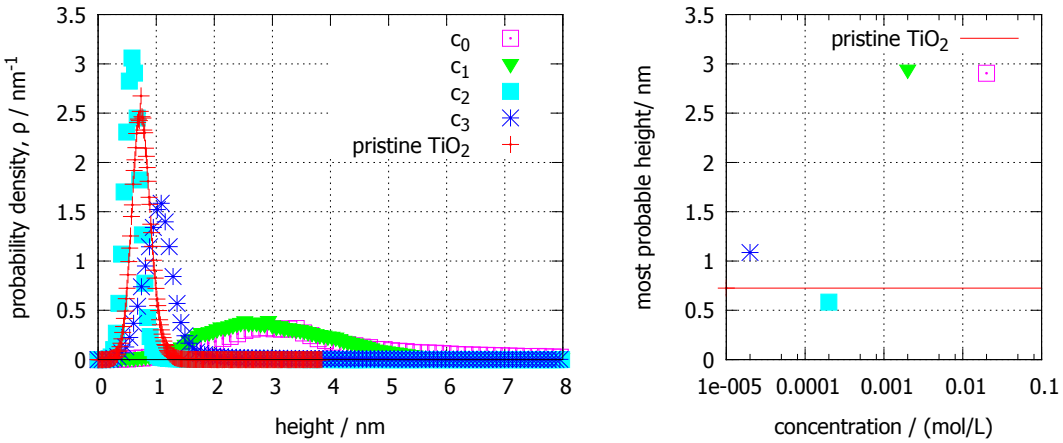

(a) Height distributions (b) Most probable height

Figure 14.: Precursor concentration dependent topographic properties for: $c_0 = 2 \times 10^{-2}\,\mathrm{mol/L}$, $c_1 = 2 \times 10^{-3}\,\mathrm{mol/L}$, $c_2 = 2 \times 10^{-4}\,\mathrm{mol/L}$, and $c_3 = 2 \times 10^{-5}\,\mathrm{mol/L}$

layer can not be determined from this data obtained by tapping mode atomic force microscopy.

Before the concentration dependent experiments were conducted and evaluated an easy to exploit relationship between between concentration and number of quantum dots per unit area was hoped to be found. Unfortunately this relationship was not obtained. With such a relationship it would have been perhaps possible to predictably prepare samples with isolated quantum dots. However, one sample of merit with well isolated quantum dots, mimicking results from expensive epitaxial methods like molecular beam epitaxy, was obtained from a two cycle SILAR process. The outstanding properties of this sample of isolated quantum dots and its differences from the synthesis of the other sample are the content of the following section 2.4. On the other hand one should recall the calculated phase digram of the different epitaxial growth models as function of surface coverage and lattice mismatch which was presented as Figure 7, page 9. As AFM only measures relative heights, one can speculate that low precursor concentrations might result in a Frank-van der Merwe like growth mechanism, FM in Figure 7, giving a flat lead sulfide thin film. High precursor concentrations might result in phases with riping, R_1 to R_3 in Figure 7, consisting of particles with different sizes and heights.

Conclusions about Concentration Dependence *The quantum dot size is influenced by the precursor concentration in the investigated range of dilution. Apparently there is a threshold concentration below which the nucleation of lead sulfide quantum dots is hindered on the rutile (100) face. For processing many samples one should therefore steadily control the precursor concentration and prevent it from dropping below this*

threshold concentration. On the other hand very high concentrations may not be completely advantageous, so resources can be saved by lowering the concentration to a value not that far above the apparent concentration threshold. Such a just above threshold concentration, when compared to a very high concentration, may spare time as it is faster prepared by a quicker dissolution of the precursors; may save precursor material from the start if it is not consumed down to the threshold concentration; may produce less waste if it is not consumed down to the threshold concentration. The point of depleting and therefore generating waste might be circumvented in larger scale applications by adding fresh precursor salts to the existing solution, or by partial removal of solvent to increase the concentration to a level above the threshold. With some care that might even be done without interrupting the production process. In contrast exchanging the source, for example in a molecular beam epitaxy setup, will for sure interrupt any running process.

2.4. Sample of Isolated Quantum Dots

2.4.1 Proof of Concept: Isolated Quantum Dots

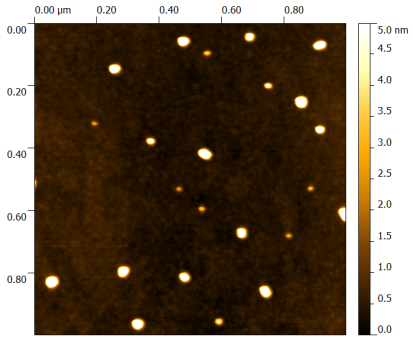

Figure 15.: AFM: Isolated PbS QDs from 2 cycles SILAR

To synthesize separated lead sulfide quantum dots, the general method in appendix A.1 on page 53 was followed with the following changes: Methanol was not deoxygenated before the precursor solutions were prepared, instead the precursor solutions and the methanol for the rinsing baths were deoxygenated just before the SILAR process, which happened four days after the $Pb(NO_3)_2$ and Na_2S precursor solutions were prepared. In contrast to the other samples the titanium dioxide sample was used as received from the manufacturer[1]. All other samples presented in this work were subject to atomic force microscope studies before the SILAR process was applied to them. This also involved glue removal from the samples' backsides using sonication in an acetone bath, see appendix B.1.1, page 58, for details. The conditions for this experiment are summarized in Table 5.

[1]Crystal GmbH, Ostendstr. 25, 12459 Berlin, `http://www.crystal-gmbh.com`

Table 5.: SILAR conditions for isolated quantum dots

Step	No. of cycles	Immersion time / s	Concentration
Wetting		5	
Pb^{2+}	2	20	$0.02\,\mathrm{mol/L} = c_0$
Rinse I	2	30	
S^{2-}	2	20	$0.02\,\mathrm{mol/L} = c_0$
Rinse II	2	20	
Rinse III		50	

Conclusions about Proof of Concept *Isolated quantum dots can be fabricated on a titanium dioxide substrate by using a lead sulfide SILAR process. A very clean surface seems to be important. Employing an acetone based cleaning procedure proved to be not good enough. For experiments connected with the rutile surface for example Jang* et al. *used a more rigorous cleaning procedure.[28] Their procedures consists of sonication in three different solvents, annealing for* 2 h *at* 550 °C *and etching with* aqua regia. *On the other hand one might speculate that acetone based cleaning alters the titanium dioxide surface in an unexpected way, for example favoring a titanium or oxygen rich surface. A change in surface composition could be a possible reason for the different results obtained from acetone cleaned substrates and from samples prepared on as received substrates.*

2.4.2 Elemental Composition of Quantum Dots

Eight weeks after the sample preparation scanning electron microscopy (SEM) and energy dispersive X-ray spectroscopy (EDX) were performed on the sample exhibiting isolated quantum dots. One week after, atomic force microscopy (AFM) in tapping mode was employed to get topographic information about the sample.

Figure 16a shows a scanning electron microscope micrograph of six isolated quantum dots. From the quantum dot that appears brightest in the SEM micrograph an EDX spectrum was recorded with 600 s integration time. The area probed for that EDX spetrum is indicated by a yellow circle in Figure 16a, the resulting spectrum is depicted in Figure 16b. X-ray emission lines from various elements are included in the plot, their height representing their relative intensity. Close to 2.3 keV sulfur and lead have their most intense X-ray emission lines. In addition both lead and sulfur have secondary X-ray emission lines with about 2.45 keV energy. This overlap of the X-ray emission lines is problematic for quantifying the ratio of sulfur to lead in the sample. However, in the spectrum presented in Figure 16b X-ray emission is evidently above the noise level in the range of 2.2 keV to 2.6 keV, which may indicate lead and sulfur. Sulfur has in addition another X-ray emission line at about 0.15 keV. This low energy line of sulfur should not be used for quantifying the sulfur content, its energy is so low, that it will get absorbed by the detector window. The detector windows, on the other hand, is

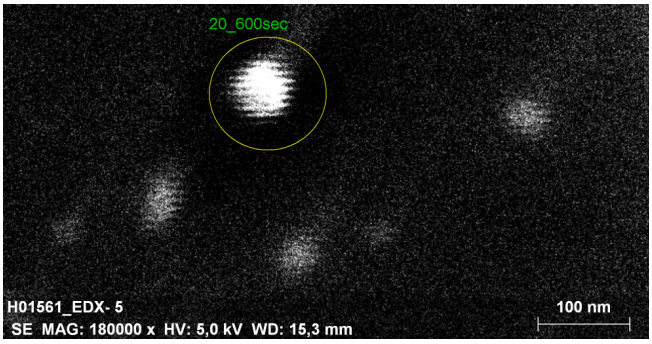

(a) SEM with several quantum dots

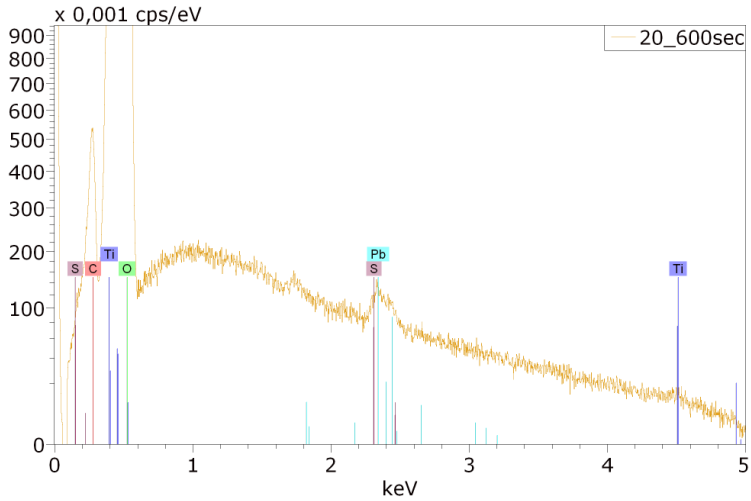

(b) EDX spectrum of area encircled yellow in Figure 16a, 600 s integration time

Figure 16.: SEM and EDX of sample with isolated quantum dots

made from polycarbonate. Therefore, X-ray autofluorescence from oxygen and carbon can be expected when the detector window is hit by X-ray with energies higher than those of the low energy oxygen and carbon X-ray emission lines. In addition X-ray autofluorescence from the silicon in the detector itself can be expected. Silicon has an X-ray emission line at 1.8 keV.

Because of the aforementioned overlap of the lead and sulfur X-ray emission lines it is not possible to determine their elemental ratio with confidence. Furthermore with the settings used for this EDX experiment the electron beam is expected to penetrate 200 nm deep into the surface. With this penetration depth mainly the titanium dioxide substrate will be probed as the quantum dot is expected to be thinner than ten nanometers. The quantum dot height will be estimated later on in subsection 2.4.4, page 34. Having these limitation in mind the spectrum presented in Figure 16b was fitted taking the following elements into account: lead, sulfur, silicon, titanium, oxygen, carbon. Results of the fitting are presented in Table 6.

Table 6.: Elemental composition of a quantum dot from EDX (Figure 16b)

	Atom %	Weight %	Error of weight % (3σ)
Lead	0.12	0.99	0.08
Sulfur	0.05	0.07	0.03
Silicon	0.17	0.19	0.04
Titanium	27.26	52.43	5.65
Oxygen	71.05	45.67	4.8
Carbon	1.35	0.65	0.11

The quantification of oxygen besides titanium also suffers from an overlap of X-ray emission lines of those two elements at about 0.5 keV, especially as oxygen has only this one overlapping X-ray emission line in the probed energetic region of 0 keV to 5 keV.

With all the mentioned difficulties and shortcomings all numbers in Table 6 should be considered with great care, and therefore any conclusion drawn from them is highly speculative. An example for the inaccuracy of the performed fitting is the discrepancy of the expected titanium to oxygen ratio. With a penetration depth of the electron beam of about 200 nm and an assumed quantum dot height of 10 nm about 95 % of the probed volume are expected to be made out of titanium dioxide. In fact titanium and oxygen contribute 98.31 % to the atomic composition and 98.1 % to the weight. But the estimated atomic ratio titanium to oxygen from the fitting is 1:2.6. This ratio is quite off from the expected ratio of 1:2 for titanium dioxide (TiO_2). Considering the mentioned problem of overlapping X-ray emission lines for titanium and oxygen, the large deviation from expected stoichiometry to estimated stoichiometry of titanium dioxide may be attributed to the overlap of their respective X-ray emission lines.

The situation for lead and sulfur is similar to the situation for titanium and oxygen. From Table 6 we get an atomic ratio of sulfur to lead of 1:2.4. For lead sulfide (PbS) a ratio of 1:1 would be expected for crystalline lead sulfide quantum dots. Here expected and calculated value differ hugely. Because of the already presented doubts due to X-ray emission line overlap one can not derive the presence of lead sulfide. One might speculate that there is a small amount of lead sulfide present, but the majority of lead is present as lead oxide, though this is not supported by any evidence. Another speculative understanding could be that there is no sulfur at all present and the complete signal around 2.2 keV to 2.6 keV needs to be assigned only to lead.

Traces of silicon and carbon identified from this spectrum are tentatively assigned to partly stem from autofluorescence of the detector and detector window. Another part of the silicon and carbon signal might be due to pollution of the sample. The sample was prepared with organic solvent solution, of which carbon is the main component.

If one would like to draw any conclusion from the presented facts and speculations it should be that EDX is not able to prove the existence of lead sulfide quantum dots on a titanium dioxide surface without doubt. The overlap of X-ray emission lines of lead and sulfur prevents deriving meaningful data about the elemental composition and the

penetration depths of the electron beam leads to probing a large amount of substrate compared to the amount of material probed within the quantum dot. In any case, the continuous nucleation versus number of cycles investigated in section 2.2, page 16, might serve as an indication of depositing stoichiometric lead sulfide, following a there described layer-wise deposition mechanism. This is also supported by the fact that working lead sulfide quantum dot sensitized solar cells can be fabricated using SILAR.

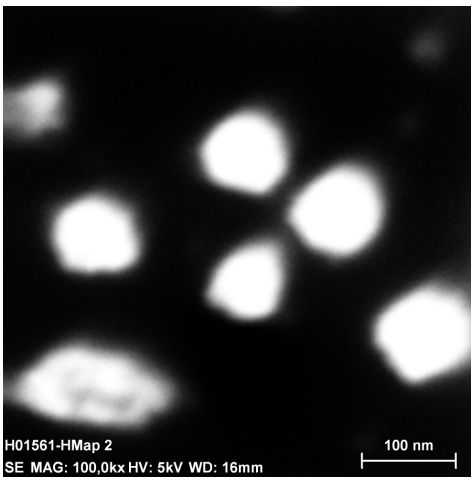

(a) SEM

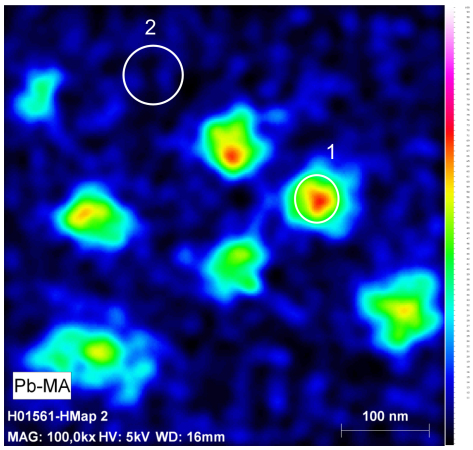

(b) EDX elemental map: lead, white circles and numbers mark areas from which EDX spectra were derived

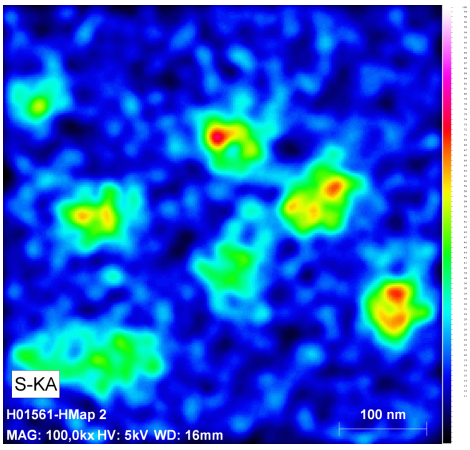

(c) EDX elemental map: sulfur

Figure 17.: SEM image and EDX elemental maps of QDs from 2 cycles PbS SILAR

Another way to do elemental analysis is to record hypermaps. For generating a hypermap the EDX spectra for each pixel in an SEM micrograph are recorded. A hypermap has been recorded for the area shown in Figure 17a. To derive an elemental map from a hypermap for each pixel the number of counts from a specific X-ray emission

line of the element in question is used to generate a new map. The elemental maps for the main lead X-ray emission line is shown in Figure 17b and the elemental map for the main sulfur X-ray emission line is shown in Figure 17c. The elemental maps were extracted and deconvoluted as described by Salge and Terborg in reference [29]. The color scale bar in the elemental maps covers the total range of the element's abundance in the measured area. Going from lowest element content, in black, to highest element content measured, in purple and white.

As mentioned before the X-ray emission lines of lead and sulfur are close to each other in energy. Therefore it is not surprising to find the presented elemental maps exhibiting very similar distributions of lead and sulfur on the substrate surface. From the elemental maps shown it may be very intriguing to conclude that were lead is, there also is sulfur, but this should not be done. The way the elemental maps are generated from EDX data automatically should lead to similar maps for sulfur and lead whenever there is lead or sulfur in a sample.

From the recorded hypermap one can also derive classical EDX spectra. Figure 18 shows a typical EDX spectrum of a quantum dot, the area used for generating this EDX spectrum is marked as 1 and with a white circle in Figure 17b. X-ray emission lines from various elements are included in the plot, their height representing their relative intensity.

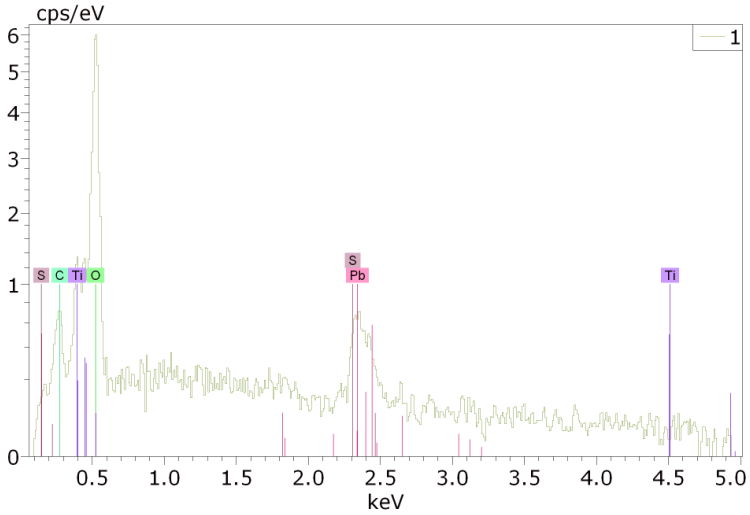

Figure 18.: Quantum dot, 1 in Figure 17b

The shown EDX spectrum of quantum dot derived from a hypermap (Figure 18) exhibits in general the same features as the conventionally obtained EDX spectrum of a quantum dot already shown in Figure 16b, page 28. Though one has to notice that the energy resolution of the hypermap derived data is lower.

For this derived EDX spectra all concerns and problems apply that were already discussed with the conventionally measured EDX spectra of a quantum dot presented in Figure 16b on page 28. As the same concerns apply the values derived from fitting

the hypermap derived EDX spectrum are also subject to great suspicion. Nonetheless the result of fitting the spectrum shown in Figure 18 is summarized in Table 7.

Table 7.: Elemental composition of a quantum dot from EDX hypermap (Figure 16b)

	Atom %	Weight %	Error of weight % (3σ)
Lead	0.54	4.32	0.25
Sulfur	0.19	0.24	0.04
Silicon	0.36	0.39	0.05
Titanium	27.54	51.09	5.72
Oxygen	69.57	43.13	4.65
Carbon	1.81	0.84	0.14

The results presented in Table 7 should be considered with the same great caution as the results from the conventional EDX spectra shown in Table 6, page 29. As the results here are analog to the results from the conventional EDX spectra (Figure 16b, page 28)the reader is referred to the discussion there. Here only a short summary will be given: Oxygen and titanium are the major constituents of the sample, providing 97.11 % of the atomic content. Lead and sulfur are identified in traces, but telling them apart is questionable. Silicon and carbon were also identified. Atomic ratio of sulfur to lead is 1:2.8, the ratio of titanium to oxygen is 1:2.5.

From the hypermap presented in Figure 17 an EDX spectrum was derived probing a part of the substrate surface that is not covered by a quantum dot. The area used to derive this EDX spectrum is marked with 2 and a white circle in Figure 17b. The resulting EDX spectrum is presented in Figure 19. There is no signal showing up from

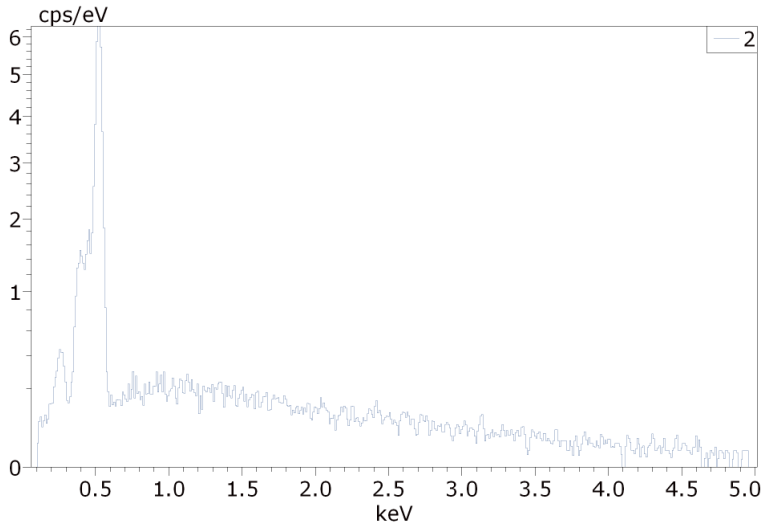

Figure 19.: Inter quantum dot space, 2 in Figure 17b

the noise in the range from 2.2 keV to 2.6 keV. Because of that one could argue that there is neither sulfur nor lead on the substrate surface between the quantum dots. On the other hand the signal of a wetting layer like coating of lead sulfide would be very weak. What this observation suggests is that the composition of quantum dots differs from the area between quantum dots. Quantum dots might contain lead or sulfur, or both, whereas the area free of quantum dots might be lead and sulfur free.

Conclusions about Elemental Composition of Quantum Dots *The elemental composition of quantum dots could be revealed with scanning electron microscopy (SEM) and energy dispersive X-ray spectroscopy (EDX) to consist of lead and/or sulfur. The exact stoichiometry of the quantum dots could not be derived from SEM and EDX measurements. What could be concluded is that the composition of the bare surface does not match the quantum dot composition. Quantum dots might consist of lead and sulfur but telling lead and sulfur apart and quantifying the amount of lead and sulfur in a quantum dot was not possible. Because of the difficulties due to overlapping X-ray emission lines, a method not relying on characteristic X-ray emissions should be used in further studies of the sample with isolated quantum dots. A method of choice could be secondary ion mass spectrometry (SIMS), it uses atomic mass spectroscopy to identify elements emitted from a substrate that is bombarded with ions. As SIMS is more surface specific with penetration depths of only several nanometers it might also answer the question of a wetting layer in between the quantum dots.*

2.4.3 Quantum Dot Surface Distribution

In section 1.1 it was mentioned that quantum dots are efficient light absorbers. For a working device like a solar cell a high areal number density of quantum dots n_a is desirable. According to Equation 11 the count of quantum dots N residing on an area A are needed to be known to calculate the areal number density n_a

$$n_\mathrm{a} = \frac{N}{A}. \tag{11}$$

To determine the needed numbers the atomic force microscope image of isolated quantum dots presented in Figure 15 and three similar ones from the same sample where analyzed. In the computer software `Gwyddion` (see appendix C.1, page 60) quantum dots were marked with a *mask* by employing the `Mark by Threshold` routine with appropriate height and slope thresholds, respectively. Where necessary the mask was tweaked by hand using the `Mask Editor`, for example to remove single pixels that were identified erroneously as quantum dots by the `Mark by Threshold` routine. Various `Grain Statistics` like the *Number of grains* were then exported into text files for convenience and further processing.

On the four 1 µm by 1 µm areas investigated 18, 27, 23 and 29 quantum dots were identified respectively. Averaging those yields the areal number density of $n_\mathrm{a} = (2.4 \pm 0.5) \times 10^9\,\mathrm{cm}^{-2}$. Using this one can use Equation 12 to calculate the average

inter particle distance d_{ip}. This assumes a square lattice of quantum dots to model the position of quantum dots.

$$d_{\mathrm{ip}} = \frac{1}{\sqrt{n_{\mathrm{a}}}} \tag{12}$$

For the sample investigated the inter particle distance is $d_{\mathrm{ip}} = (2.0 \pm 0.2) \times 10^{-7}\,\mathrm{m}$; that is roughly 200 nm.

For various epitaxially grown quantum dots areal number density in the range of $1 \times 10^{10}\,\mathrm{cm}^{-2}$ to $1 \times 10^{12}\,\mathrm{cm}^{-2}$ are reported in literature.[30, 31, 12, pp. 18, 27, 85] With $(2.4 \pm 0.5) \times 10^{9}\,\mathrm{cm}^{-2}$ the here measured density is four to five times smaller than the low density sample reported by Schneider *et al.*[30] This is not an alarming fact, a lot of time has been spent by many groups to optimize the areal number density in epitaxially grown quantum dots. The SILAR method to grow quantum dots on flat substrates presented in this work has not yet had the chance to be optimized as it is rather new. In a very recent publication from spring 2013 Lee *et al.* claim to get an areal number density of about $0.95 \times 10^{11}\,\mathrm{cm}^{-2}$ from an aqueous SILAR process on mesoporous titanium dioxide.[32] Lee *et al.* added 1 mol/L triethanolamine to the lead containing cationic precursor solution to increase the areal number density of quantum dots. In this respect controlling the number of deposited quantum dots per unit area on flat surfaces might also be achieved by adding additives like triethanolamine to the precursor solutions.

Areal number density is assumed to be homogeneous over four measurements that were performed at different spots of the sample. This is supported by the observation of homogeneity in large areas probed by scanning electron microscopy. This scanning electron microscopy data presented later in subsection 2.5.2.

Having now established the existence of quantum dots on this up to now unique sample, it is interesting to have a look at their individual properties. Using their spatial dimensions diameter and height one can assess if a quantum dot actually should show quantum confinement as it was presented in section 1.2, page 6. Also the aspect ratio is of interest as a measure for the general shape of a quantum dot.

Conclusions about Quantum Dot Surface Distribution *For the sample of isolated quantum dots presented here the quantum dots are assumed to be homogeneously distributed over the complete sample surface. The areal number density of these proof of concept SILAR quantum dots is four times smaller than values from well optimized recipes of molecular beam epitaxy and metal organic chemical vapor deposition. At least one research group claims to already have increased the areal number density of SILAR grown quantum dots on mesoporous titanium dioxide. In future research one might try to follow their example to increase the areal number density by also adding triethanolamine to the lead precursor solution.*

2.4.4 Quantum Dot Aspect Ratio

To calculate the aspect ratio of the already marked quantum dots the following two `Grain Distributions` were exported from the computer software `Gwyddion`: *Equiva-*

lent disc radius r_{eq} and *Grain height* Δz. The *Grain height* is a user defined function implemented as described in appendix C.1, page 60. For the equivalent disc radius internally the area of a grain in pixels is computed. Then the radius of a disc having this particular area is calculated.

The resulting data from the four measurements were combined and the diameter of each quantum dot was calculated from the equivalent disc radius: $d = 2 \times r_{\mathrm{eq}}$. The average diameter was found to be $(3.2 \pm 1.3) \times 10^{-8}\,\mathrm{m}$. A histogram of all obtained

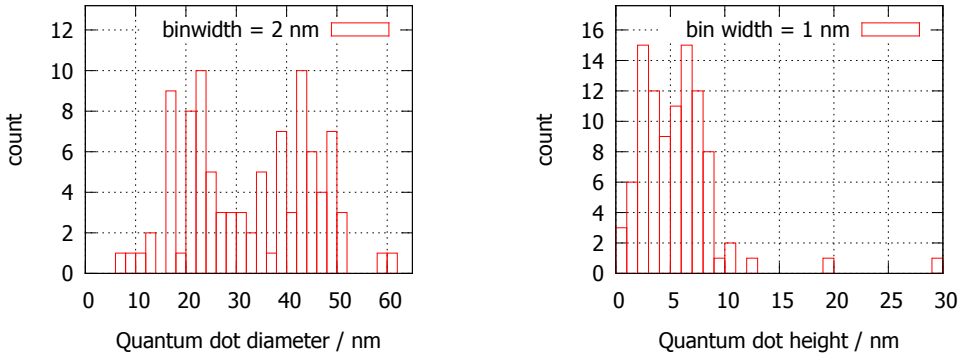

(a) Diameters (b) Heights

Figure 20.: Histograms of quantum dot dimensions

quantum dot diameters is shown in Figure 20a. The high standard deviation of the diameters found $1.3 \times 10^{-8}\,\mathrm{m}$ is reflected in the broad distribution of diameters found. On the other hand two strongly preferred diameters are seen. This bimodal distribution, with its two centers at about 20 nm and 45 nm, gives an explanation to the high standard deviation, which is nearly half the value of the average diameter. Furthermore this leads the average diameter's value to be at a minimum of the distribution. Therefore the average size of quantum dot should be used only with great care. An ensemble of quantum dots with such a bimodal distribution will for example expose multiple absorption bands and fluorescence peaks, and not one centered around the averaged value. However, in section 1.2 it was stated that quantum confinement for lead sulfide should only be observed for objects smaller than 23.5 nm. In the measured samples this is only true for a small fraction of quantum dots when the diameter is considered. When height is considered nearly all examined quantum dot fulfill the criterion of being smaller than 23.5 nm and therefore quantum confinement is expected.

Figure 20b holds the histogram plot of the measured quantum dot heights, exhibiting a bimodal distribution as already seen for the quantum dot diameter. The average quantum dot height was found to be $(5.5 \pm 3.8) \times 10^{-9}\,\mathrm{m}$. Again the broad distribution of heights with two preferred height regimes leads to an unreliable average value with a large standard error.

Finally the aspect ratio $a.r. = \frac{\Delta z}{d}$ was calculated for all quantum dots and plotted as a histogram which is shown in Figure 21. The average of the aspect ratio was 0.16 ± 0.08. The histogram shown does, compared to the height and diame-

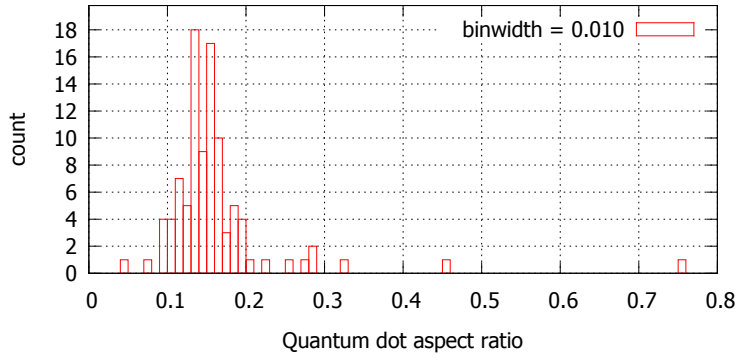

Figure 21.: Histograms of quantum dot aspect ratios

ter histograms in Figure 20, not show strong bimodal characteristics. But again the distribution is broad.

From the three presented histograms one can conclude that the synthesized quantum dots are split into two fractions. One with the quantum dots smaller in size and height and another with quantum dots larger in size and height. Both fractions share the same broad aspect ratio distribution. To have the same aspect ratio both fractions must have a linear correlation between the height and the diameter of a quantum dot. The reader may be referred back to the atomic force microscopy image Figure 15 on page 26, where clearly the two different types of quantum dot can be differentiated.

Bimodal distributions were found many times in quantum dots grown by metal-organic vapor-phase epitaxy (MOVPE) and molecular beam epitaxy.[33, 34, 35] For those two methods just mentioned bimodal distributions may be prevented by carefully controlling growth conditions like the material flux and substrate temperature. Furthermore bimodal distributions of quantum dots are predicted as phases R_2 and R_3 in the calculated phase diagram from Daruka *et al.* shown in Figure 7 on page 9.[9]

One possible reason for the two fractions of quantum dots might be the fact that two cycles SILAR were performed. Quantum dots formed during the first cycle continue to grow during the second cycle, keeping their aspect ratio constant. The second fraction of quantum dots might be grown only during either the first or the second cycle. From the available data it is not possible to say if the quantum dots of the smaller size fraction have stopped growing after the first cycle, or if they started growing delayed with the second cycle. The third perhaps most appealing explanation could be provided by an intermediate growth mechanism. In the case of an proposed intermediate growth mechanism nucleation would take place during both SILAR cycles and not only during one.

Conclusions about Quantum Dot Aspect Ratio *Although the aspect ratio was found to be identical for most quantum dots, their diameter and height is a bimodal distribution. This suggest that there might be two different growth modes, both leading to lens shaped quantum dots after two cycles SILAR, but result in two different sizes of the*

quantum dots. This might be useful when two sizes of quantum dots are desired, for example a cyan light emitting diode can be constructed out of differently sized quantum dots emitting blue and green light. If it hypothetically would be achievable to also add a third size of quantum dots emitting at a red wavelength, just by increasing the number of SILAR cycles to three, the resulting device would emit white light, which still is not trivial to do today for light emitting diodes. Though for other devices like lasers a narrow distribution with only one peak is favorable. However, more work on this is necessary to study the nucleation mechanism and its influence on the size distributions. The phase diagram in Figure 7 on page 9 might be a guide to the complexity of relating nucleation mechanisms to size distributions.

2.5. Quantum Rods

Alongside the quantum dots presented in section 2.4 elongated rod-like structures were found on the same sample. This indicates that from the synthesis of isolated quantum dots which was already presented in subsection 2.4.1, page 26 also quantum rods can be synthesized.

Conclusions about Quantum Rods *Quantum rods can be obtained by SILAR. This is the very first observation of rods grown from lead sulfide using SILAR. The quantum rods unexpectedly evolved parallel to the quantum dots. Now a naturally next challenge is to study the question: Is it possible to grow them without also growing quantum dots? And vice versa: How can the rod growth be prevented to only get quantum dots?*

2.5.1 Elemental Composition of Quantum Rods

Energy dispersive X-ray spectroscopy was employed to investigate the found quantum rods. From the experience of investigating quantum dots in subsection 2.4.2, page 27, it is clear that the determination of the quantum rod atomic composition will be ambiguous. The EDX data will therefore be presented and discussed only briefly, always with the strong doubts already expressed in subsection 2.4.2.

A resulting scanning electron microscope (SEM) image is shown in Figure 22a. For the area of this SEM image a hypermap was recorded. An elemental map for lead is presented in Figure 22b and an elemental map for sulfur is depicted in Figure 22.

Again the spatial agreement of the two elemental maps can be attributed to the way they were generated from the measured hypermap, please see subsection 2.4.2 for details.

EDX spectra for selected areas were extracted as described in subsection 2.4.2. An EDX spectrum for a quantum dot is shown in Figure 23. This spectrum of a quantum rod exhibits the same features as an EDX spectrum of a quantum dot already discussed in subsection 2.4.2. Therefore one can tentatively assume that the quantum rods are of similar composition as the quantum dots. As the exact composition of the quantum dots could not be obtained in subsection 2.4.2, for reasons presented there, corresponding calculations for the quantum rods were not performed.

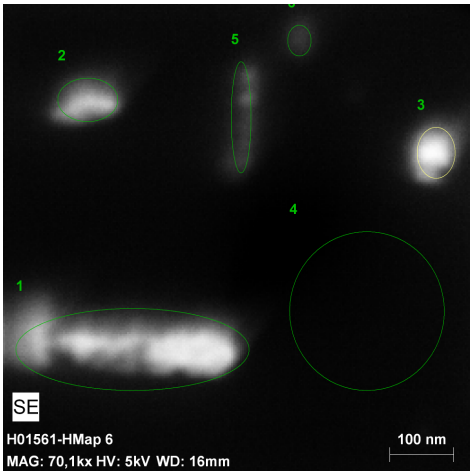

(a) SEM

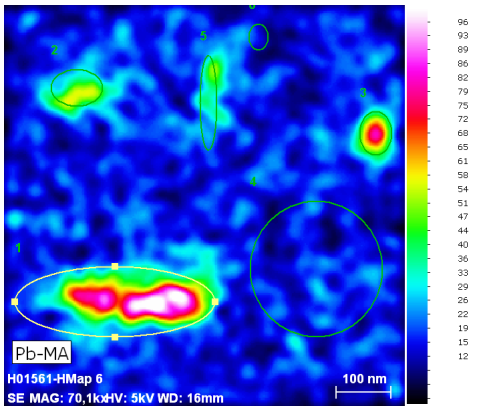

(b) EDX elemental map: lead

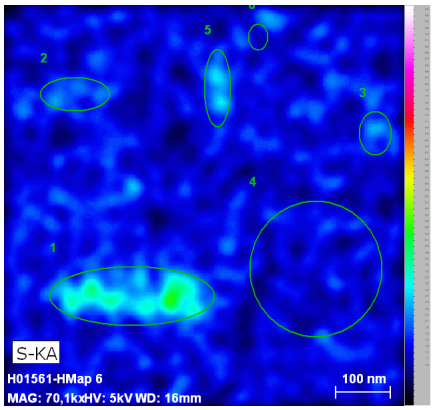

(c) EDX elemental map: sulfur

Figure 22.: SEM image and EDX elemental maps of rods from 2 cycles PbS SILAR

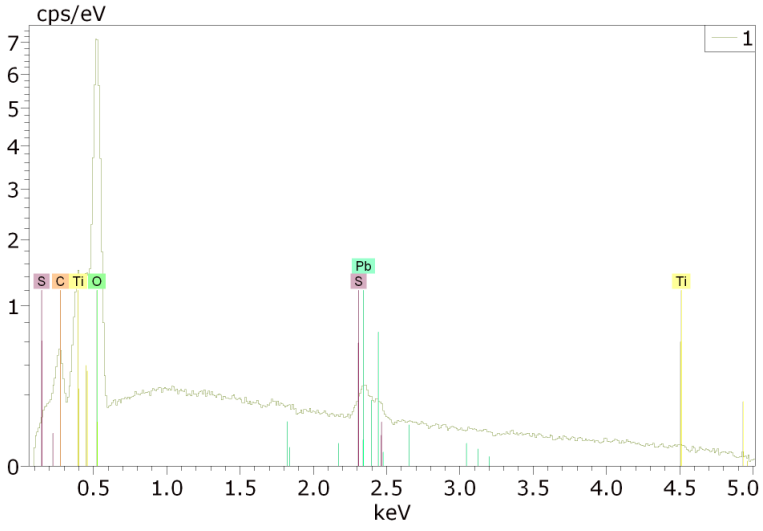

Figure 23.: EDX from hypermap: quantum rod, 1 in Figure 22

The area free of quantum rods and dots which is carrying a 4 in Figure 22, was also used to extract an EDX spectrum. This spectrum of plain substrate is shown in Figure 24. Again, in the range from 2.2 keV to 2.6 keV only noise is seen. From that

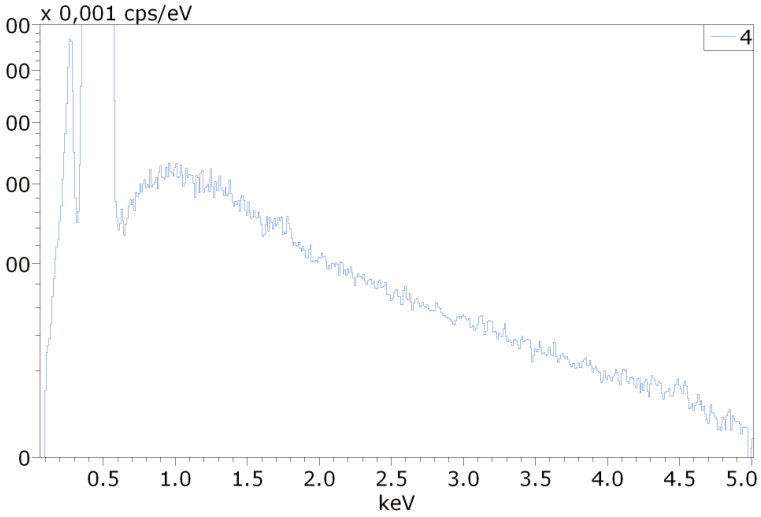

Figure 24.: EDX from hypermap: plain substrate, 4 in Figure 22

one might conclude that lead and sulfur are both not present in this investigated area. Signals of titanium, carbon and oxygen on the other hand are present. Overall the main important features of this spectrum (Figure 24) are similar to the EDX spectrum one of plain substrate already presented as Figure 19 on page 32. Therefore the detailed discussion in subsection 2.4.2 might be also applied to this spectrum.

Conclusions about Elemental Composition of Quantum Rods *The conclusions for the elemental composition of quantum rods are analog to those for the quantum rods, presented at the end of subsection 2.4.2: The elemental composition of quantum rods could not be revealed with scanning electron microscopy and energy dispersive X-ray spectroscopy. What possibly could be concluded is that the composition of the quantum rods is similar to the quantum dot composition: Quantum rods might consist of lead and sulfur but telling lead and sulfur apart and quantifying the amount of lead and sulfur in a quantum rod was not possible. Because of the difficulties with the overlapping X-ray emission lines, a method not relying on characteristic X-ray emissions should be used in further studies of quantum rods. A method of choice could be secondary ion mass spectrometry (SIMS), it uses atomic mass spectroscopy to identify elements emitted from a substrate that is bombarded with ions. As SIMS is more surface specific with penetration depths of only several nanometers it might also answer the question of a wetting layer in between the quantum dots and rods.*

2.5.2 Topography of Quantum Rods

A typical example of a found rod's atomic force microscope tapping mode height image is presented in Figure 25. For this atomic force microscope image it is important to note, that the height scale bar is from 0 nm to 50 nm, it exhibits a ten times larger range than the images presented in the preceding parts of this work, where usually a maximum height of 5 nm was sufficient to show the captured features. Length and width of such a quantum rod can be measured manually within the computer program `Gwyddion` using the `Distance Tool`, or more convenient using the `Grain Measurement Tool`. For that the to be analyzed rods need to be marked by a mask. This is done in the same way as quantum dots were selected for analysis in subsection 2.4.3, page 33. After the masking, single quantum rods can be analyzed with the `Grain Measurement Tool`, or the analysis results of all marked rods can be exported via the `Grain Statistics` function from the `Data Process` menu. Here the *Minimum bounding size*, gives the width, the *Maximum bounding size*, holds the length, and the user defined function *Grain height* stores the height of the rods. How *Grain height* was implemented is available in appendix C.1, page 60.

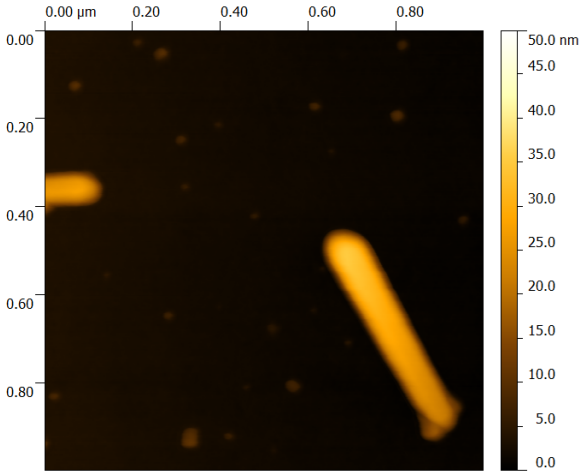

Figure 25.: AFM: Rods after 2 cycles, c_0, PbS SILAR

The rod shown in Figure 25 is found to be 128 nm wide, 548 nm long and 34 nm high. Additionally it shows a slope over the long axis, from low in the bottom of the image to high in the upper part of the image. Also to note are the two smaller particles at the lower end of the rod. One might believe that the rod started to grow from two quantum dots very close to another. In general the rods show a random orientation, pointing with their long axis into all different directions. Widths lie in the range of 80 nm to 150 nm and lengths of 250 nm to 550 nm. Heights of rods cover a range from 20 nm to 50 nm. The quantum rods are less densely distributed on the sample surface than normal quantum dots: areas as large as 1 µm by 1 µm can be found without any rods. On the other hand their density is homogeneous over the complete sample area. A high

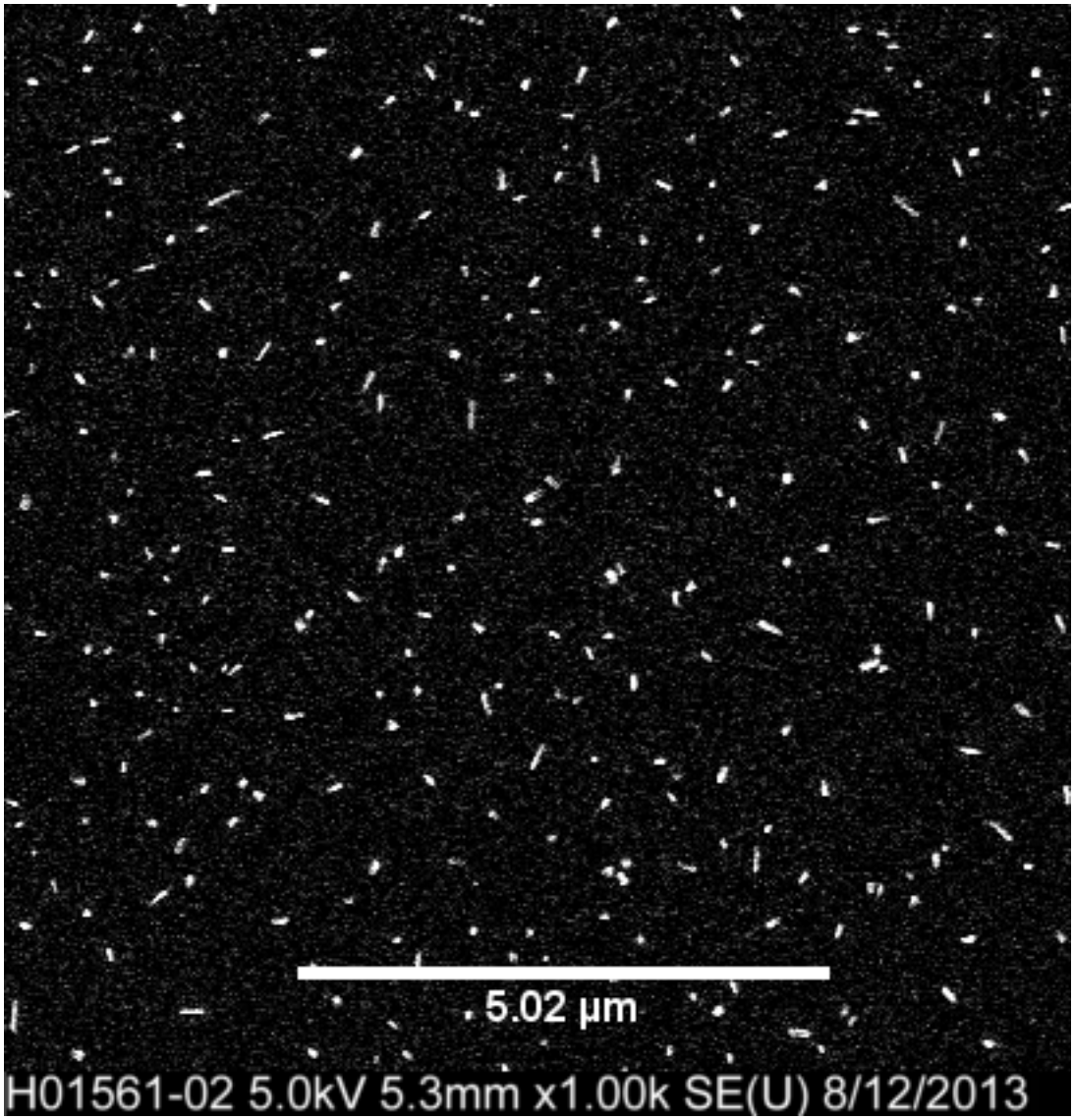

Figure 26.: SEM: Quantum rods homogeneously distributed and randomly oriented

resolution, large area 125 µm by 87 µm scanning electron microscope image showing the homogeneous coverage and further scanning electron images taken at various positions support the homogeneity of the rods distribution on the surface. A random 20 µm by 20 µm crop of this large image is shown in Figure 26.

The larger rod-like structures are prominent, small quantum dots are present in the form of tiny white dots everywhere.

Conclusions about Topography of Quantum Rods *Quantum Rods often exhibit bulges at one of their ends, there is the possibility that the rod growth was nucleated by quantum dots. Height of the quantum rods is comparable to quantum dot diameter. The length, width and height of quantum rods varies largely, but their distribution over the sampled area seems to be homogeneous. Their height well exceeds the amount of material expected to be deposited during the two performed SILAR cycles on top of a surface. So either a different adsorption mechanism might be in place during the immersion into the precursor solution, or already deposited material might get rearranged to form rods during the rinsing steps. The majority of the rods might not show quantum confinement as their smallest dimension often is larger then the lead sulfide exiton Bohr radius.*

2.6. Spectroscopic Attempts

Quantum confinement in quantum dots results in optical and electronic properties of the quantum dots differing from properties of bulk materials. To investigate this behavior several spectroscopic methods were employed.

2.6.1 UV-Vis Absorption

The UV-Vis absorption spectrum of the sample of isolated quantum dots presented in section 2.4 was recorded with a Perkin-Elmer Lambda 900 spectrometer. The whole spectral range accessible by the spectrometer from 250 nm to 2500 nm was probed. Only absorption by the titanium dioxide substrate could be identified. Titanium dioxide exhibits a linear napierian absorption coefficient α larger than $1 \times 10^4/\mathrm{m}$ for any wavelength below 407 nm.[36] In contrast to this, layers of isolated epitaxial quantum dots were found to possess a linear napierian absorption coefficient of $\alpha = 1 \times 10^2/\mathrm{cm}$.[37] From the values of the linear decadic absorption coefficient the napierian absorbance

$$A_\mathrm{e} = \alpha \times l \tag{13}$$

can be calculated if the absorbing path length l is known. Let's assume an absorbing path length of 10 nm for the lead sulfide quantum dot layer as this height is seldom exceeded by quantum dots presented in Figure 20b, on page 35. For the titanium dioxide substrate the absorbing path length is the thickness of the crystal $l = 0.5 \times 10^{-3}\,\mathrm{m}$. Therefore the absorbance can be calculated to $A_\mathrm{e} = 1 \times 10^{-6}$ for the quantum dot layer and to $A_\mathrm{e} = 5$ for the titanium dioxide substrate. As the absorbance of the quantum

dot layer is so small detecting any absorbance signal from the quantum dot layer will be difficult.

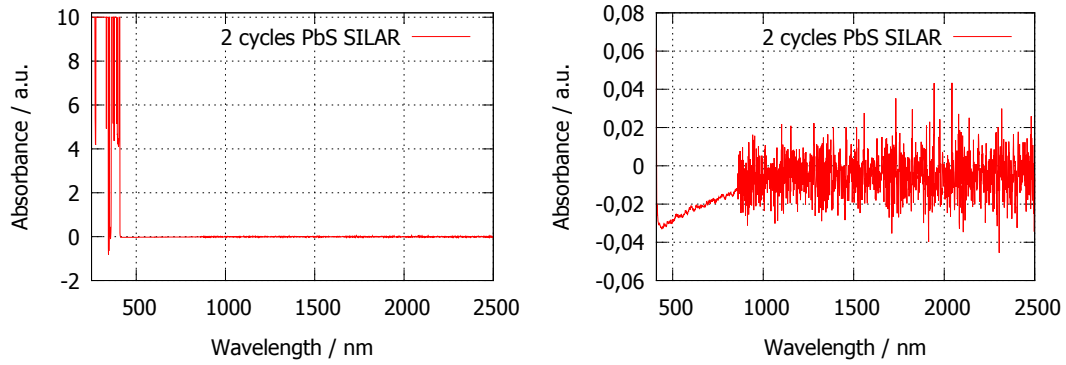

(a) Complete spectrum

(b) Zoom in above 410 nm

Figure 27.: Absorption spectrum of TiO_2 rutile substrate after 2 cycles of PbS SILAR

From Figure 27a it is clear that above 408 nm there is no absorption, whereas below 408 nm strong absorption occurs. This step like behavior of absorption is typical for bulk semiconductors. As long as an incident photon has an energy below the semiconductor's bandgap no absorption takes places. If the photon's energy exceeds the bandgap, it will be absorbed. As the density of states in the valence band and in the conductance band is continuous, the exact photon energy is not of importance as long as it is larger than the bandgap between valence and conductance band. These measured properties of rutile are in perfect agreement with literature where rutile is described as a wide bandgap semiconductor with a bandgap of 3.05 eV corresponding to a wavelength of 407 nm.[36] In subsection 2.4.4 the average quantum dot height of the measured sample was found to be $(5.5 \pm 3.8) \times 10^{-9}$ m. For colloidal lead sulfide quantum dots with a diameter of 5 nm absorption around 1400 nm has been reported in literature.[38] Lead sulfide as a bulk material has a bandgap of 0.88 eV corresponding to 3020 nm.[39] Therefore absorption features in the range from 1400 nm to 3040 nm were expected. Figure 27b does not show any absorption in the range for which quantum dot absorption feature were predicted. The change of the noise level at 900 nm is due to changing detectors within the spectrometer.

Conclusions about UV-Vis Absorption *For the one sample investigated with UV-Vis absorption it seems that UV-Vis absorptions measurements are not suitable for detecting a layer of lead sulfide quantum dots. Attenuated total reflectance might be a method to try as it usually probes the top most* 0.5 µm *to* 2 µm *of a sample and not the complete sample's thickness.*

2.6.2 Fluorescence

On a J&M TIDAS fluorometer fluorescence emission spectra of a sample used in the precursor concentration dependence experiments, section 2.3 page 22, were recorded with various excitation wavelengths. The sample used for the fluorescence measurements was subject to 5 cycles of lead sulfide SILAR using precursor solutions with concentrations $c_1 = 2 \times 10^{-3}$ mol/L as described in the appendix A.1. In this polycrystalline looking sample Figure 13b, page 24, quantum dots are not isolated and show inhomogeneity in diameter and height. Therefore this sample is by far not optimum for proving quantum confinement. As fluorescence peaks usually appear not far away from absorption peaks one can roughly estimate the expected range for light emission from quantum dots from the absorption range predicted in the previous subsection 2.6.1. With those assumptions fluorescence from quantum dots larger than 5 nm in height is predicted to be roughly found in the range from 1400 nm to 3040 nm. Furthermore the J&M TIDAS fluorometer can only detect emission wavelengths up to 1140 nm. Taking the limitations of the device into account only fluorescence from very small quantum dots will be detectable. Whatsoever, fluorescence emission spectra with excitation wavelengths of 300 nm, 400 nm, 450 nm, 500 nm and 550 nm were recorded from pristine titanium dioxide and from the sample after lead sulfide (PbS) SILAR. The recorded spectra are presented in Figure 28. Within the detectable emission wave-

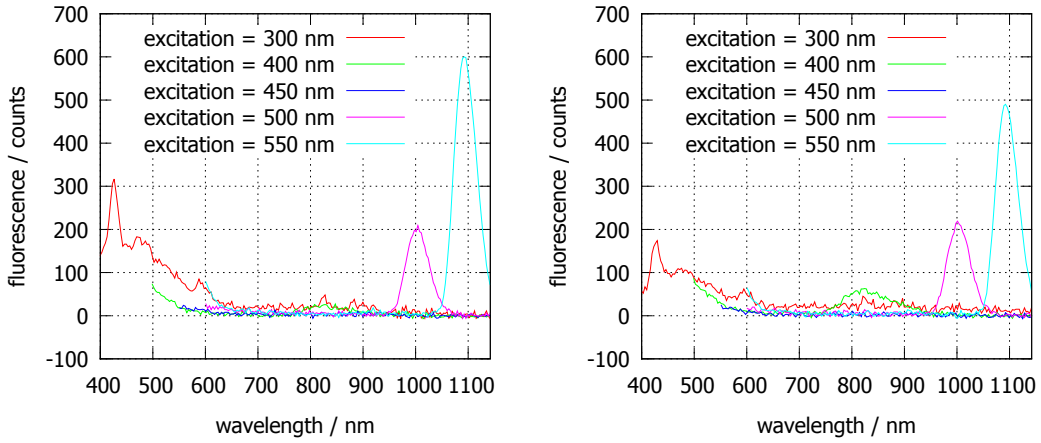

(a) Pristine titanium dioxide sample (b) Titanium dioxide sample after PbS SILAR

Figure 28.: Fluorescence emission spectra from different excitation wavelengths

length range up to 1140 nm no feature could be identified stemming from lead sulfide quantum dots. All features found in the data taken after the SILAR process (Figure 28b) are also found in the spectra of pristine titanium dioxide (Figure 28a). Most features occur at the doubled excitation frequency 600 nm, 800 nm, 90 nm, 1000 nm and 1100 nm and are probably artifacts stemming from a grating used to spread the beam onto a diode detector array in the fluorescence detector. The same argument of the beam spreader is true for the titanium dioxide fluorescence which can be found at

roughly 410 nm and 820 nm.

Conclusions about Fluorescence *On the one hand, fluorescence measurements must be repeated on the sample of isolated quantum dots as from the that sample quantum confinement is expected. On the other hand, the used equipment is not capable of identifying fluorescence expected from the sample of isolated quantum dots. Therefore cathodoluminescence measurements are planned to be performed on the sample of isolated quantum dots.*

2.6.3 Scanning Tunneling Spectroscopy

A new scanning tunneling spectroscopy (STS) setup is currently being introduced in our research group. The sample of isolated quantum dots has not yet been investigated with STS. But various other samples were measured with this new setup. From the measured imperfect samples no reproducible results were obtained.

However, the STS result of a sample prepared similar to the sample of isolated quantum dots, with two cycles of lead sulfide SILAR and precursor concentrations of $c_0 = 2 \times 10^{-2}$ mol/L is presented with red color in Figure 29. In addition a STS

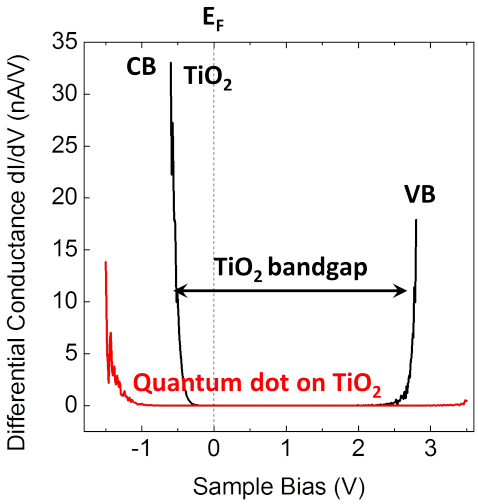

Figure 29.: STS: black: titanium dioxide (TiO_2), red: lead sulfide quantum dot, E_F: Fermi Level, CB: Conduction band, VB: Valence band, LUMO: Lowest Unoccupied Molecular Orbital

sweep of pristine titanium dioxide (TiO_2) is shown in Figure 29 using black color. On the here presented sample, that has been treated with two cycles lead sulfide SILAR, no atomic force microscopy measurements were employed, so the surface topography is not known. Furthermore, only one scan of only one quantum dot is presented. Because the STS data shown is based on only a single sweep the discussion of the STS data will

not be representative for all quantum dots, instead the following discussion can only be an example of how further measurement might possibly turn out.

The STS sweep on pristine titanium dioxide presented in Figure 29 (black color) shows that within the bandgap there are no electronic states available to inject or withdraw charges from the electronically biased sample. The differential conductance therefore is zero from about $-0.5\,\mathrm{V}$ to about $2.5\,\mathrm{V}$ sample bias. Into the conductance band electrons can be injected, the differential conductance therefore rises at a sample bias of $0.5\,\mathrm{V}$. With a sample bias larger than approximately $2.5\,\mathrm{V}$ electrons can be extracted from the valence band of titanium dioxide. From these onsets of the differential conductance one can deduce the bandgap of titanium dioxide to be approximately $3\,\mathrm{eV}$. This is in agreement with the results from UV-Vis measurements (subsection 2.6.1, page 42) and literature which provide a bandgap of $3.05\,\mathrm{eV}$ for titanium dioxide.[36]

The results of the one lead sulfide quantum dot presented in this paragraph should be considered with great care as one single measurement can not be representative for any ensemble. However, the differential conductance measured as a function of sample bias for a lead sulfide quantum dot shown in Figure 29 (red line) rises for values lower than $-1\,\mathrm{V}$. During the onset of the rise some fluctuations are visible in the differential conductance. One might attribute those fluctuations to changes in the density of states of the quantum dot. When recalling the effect of quantization on the density of states presented in section 1.2, page 6, one can conclude that electrons can be only injected into a quantum dot, when the sample bias is matched with one of the discrete energy levels of the quantum dot. Therefore, each fluctuation might be caused by a different empty electronic energy level of the quantum dot. As a result of this quantization might have been observed with STS on this quantum dot. An extraction of electrons from the highest occupied energy level of the quantum dot was not observed. Instead the differential conductance is $0\,\mathrm{nA/V}$ from $-1\,\mathrm{V}$ to $3.5\,\mathrm{V}$ sample bias. There is a minor increase of the differential conductance just before the measured range ends at $3.5\,\mathrm{V}$. But this minor increase should not attributed to anything.

Conclusions about Scanning Tunneling Spectroscopy *STS measurements on the sample of isolated quantum dots should be performed as soon as possible. The isolated quantum dots on the sample of isolated quantum dots should yield more reproducible results than the samples investigated up to now. Especially the statistical significance needs to be improved by measuring a large number of different quantum dots multiple times. However, STS might have resolved quantum confinement in a single measurement from one single quantum dot.*

3. Conclusions

This work had the purpose to gain insight into the nucleation process of quantum dots grown by successive ionic layer adsorption and reaction (SILAR), which methodology was introduced in section 1.4 page 9. The model system of lead sulfide SILAR growth on titanium dioxide rutile (100) was studied with respect to control the nucleation of quantum dots and the evolution of their properties by tuning the various parameters inherent to SILAR. Properties evaluated include spatial dimensions like diameter, height and aspect ratio, areal number densities and elemental composition. The main tool employed for following those properties was atomic force microscopy, of which a brief description is part of appendix B.1, page 56. The following SILAR conditions were checked for influence on the quantum dot properties: inert and oxidative atmosphere during SILAR, number of SILAR cycles applied, concentrations of precursor solutions, and surface cleanliness of the substrate.

Isolated quantum dots of lead sulfide were successfully synthesized using SILAR, as described in section 2.4, page 26. Spatial properties suggest similarities with other semiconductor quantum dots from established epitaxial methods. But the SILAR synthesis is more advantageous for several reasons: Neither high vacuum, nor high temperature need to be employed. No sophisticated precursor sources or expensive organometallic compounds are necessary. SILAR only needs solvents and rather cheap metal salts. One drawback is that the single crystalline substrate used is expensive and needs special treatment to be clean enough for successful quantum dot nucleation by SILAR. For established epitaxial methods, on the other hand, a crystalline clean surface is also a must have prerequisite and therefore should not be a deal breaker. The need for inert atmosphere during SILAR, at least in the investigated system, is a downside in terms of cost and practicability.

Quantum rods were observed for the first time from a lead sulfide SILAR synthesis which was shown in section 2.5, page 37.

A very clean substrate surface seems to be a main factor in successfully growing isolated nano structures on rutile (100). Another factor to consider might be the atomic surface composition, titanium and oxygen rich surfaces could invoke different nucleation mechanisms.

In the context of this work the state of the art is the one sample with isolated quantum dots. All other experiments and the preliminary conclusions drawn from these experiments were based on samples far from the current state of the art sample. Therefore it is suggested to redo all experiments presented in chapter 2, page 13, under the same condition as the sample with isolated quantum dots was prepared.

Conclusions of those results will be discussed in more detail within the following subsections.

Inert and Oxidative Atmosphere

In section 2.1, page 13 it was concluded from experiments in oxidative atmosphere and inert atmosphere that SILAR should be performed in inert air for the lead sulfide and rutile (100) system. This is a cost increasing drawback for industry. It might be worth considering if an increased transfer speed between SILAR solutions can suppress the oxidation enough so that working in oxidative atmosphere will perhaps become possible. Other combinations of substrate and coating material might not exhibit such strong effects of surface oxidation so that this problem may be circumvented in that manner. Table 1, page 10, can give some ideas which compounds have already been used in SILAR.

Cycle Dependence

From experiments on the cycle dependency in section 2.2, page 16 it was concluded that the size of semiconductor nanocrystals can be controlled in the probed model system by changing the number of SILAR cycles. The observed change in average height versus number of SILAR cycles is consistent with increasing the particle size. This observation is not surprising as it has been seen in mesoporous systems where an evident change in sample color is obtained by increasing the number of SILAR cycles. On the other hand the sample of isolated quantum dots does not show the expected height for two layers of lead sulfide. One should also note, that for non-optimal cleaned samples the growth seems to not be based on the lattice mismatch. Therefore the here applied methanolic lead sulfide SILAR method on rutile (100) surfaces should be, in its current form, limited to very few numbers of SILAR cycles. For SILAR grown lead sulfide films on various substrates Kanniainen *et al.* reported in 1996 different height increases per SILAR cycle for lead precursor solutions without and with an additional complexing agent for the Pb^{2+} ions.[27] One might try to employ this fact for further experiments on fine tuning the control on size; as the experiments of Kanniainen *et al.* did not include any sort of titanium dioxide as substrate, of course, one has to first verify that this is applicable for rutile (100) substrates.

The easy to implement size control is a key advantage of SILAR. Where in SILAR just the number of cycles needs to be counted, the effort necessary to control it in molecular beam epitaxy and the chemical vapor based methods is much higher. Often simultaneously fluxes of different reactants need to be kept stable and controlled. The flux profiles on a substrate often is not homogeneous, this fact has been used to prepare differently sized quantum dots on one substrate.[40] If this is not desired countermeasures like rotating the sample are implemented to get a narrower size distribution.

It is again important to remember that the situation may differ for other substrate-coating combinations as those have not been investigated. Should the method used in this work really mimic the the Stranski-Krastanow growth, described in section 1.3, page 6, other materials with different lattice mismatch will supposedly give other results. Overall the SILAR method needs further investigations to extend the knowl-

edge of applicable growth models. Are, for example, the three most often discussed growth models for epitaxial methods, Frank-van der Merwe, Stranski-Krastanow, and Volmer-Weber, relevant to describe growth processes in SILAR? Should this question be answered positive in the future predictions about cycle dependent properties might be possible then for SILAR. For classical epitaxial methods theoretical predictions are available and have been presented as a phase diagram of growth modes in Figure 7, page 9.[9] It would be nice to see such a phase diagram for SILAR grown quantum dots as a result of work still to be done.

Concentration Dependence

The influence of precursor concentrations on the nucleation of quantum dots was studied in section 2.3, page 22. The results showed that there apparently is a threshold concentration below which nucleation of lead sulfide quantum dots on rutile (100) does not occur. When processing many samples with the same solution, this bears the risk of depleting the solution, rendering samples to have not the expected amount of material deposited on them. Concentrations higher than the threshold yielded similar ingrowth behavior. Therefore too high concentrations might not be more advantageous than concentration just above the threshold. In practice it should be feasible to monitor the concentrations continuously and keep the precursor concentrations above the threshold while the process is running.

Elemental Composition

Energy dispersive X-ray spectroscopy (EDX) revealed the elemental composition of quantum dots in subsection 2.4.2, page 27 to be consisting of lead and/or sulfur. However, EDX was unable to identify the stoichiometric ratio of sulfur and lead in quantum dots. For identifying lead and sulfur simultaneously the sample with isolated quantum dots should be investigated with secondary ion mass spectrometry (SIMS).

In context of the elemental composition it is also of interest to know about the crystallinity of the quantum dots. With established epitaxial methods like molecular beam

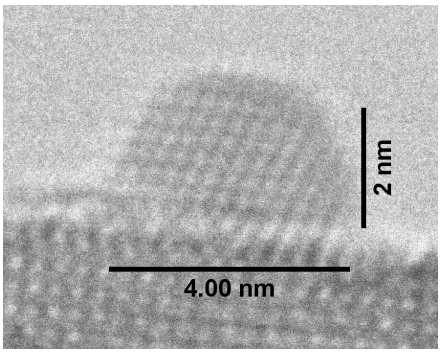

Figure 30.: TEM: Crystalline PbS QD from 6 cycles SILAR on mesoporous SnO_2

epitaxy and chemical vapor deposition, which were already presented in section 1.3, page 6, the resulting quantum dots are crystalline. For SILAR other work in our group shows that grown quantum dots are of crystalline phase. In high resolution transmission electron microscopy (TEM) the crystal lattice of lead sulfide quantum dots grown from six cycles of SILAR on mesoporous tin dioxide is resolved, see Figure 30. Therefore it is believed that the quantum dots obtained in this work are also crystalline. On the other hand the aspect ratio inFigure 30 with 0.5 differs from the quantum dot aspect ratio usually obtained in this work 0.16. One could speculate if the size of the crystallites in the mesoporous substrate influences the quantum dot aspect ratio.

Surface Distribution

In subsection 2.4.3, page 33, the distribution of the isolated quantum dots, found on one sample, was evaluated. Experimental conditions for the sample of isolated quantum dots were presented in subsection 2.4.1, page 26.

To get this result it seems to be very important to have a very clean substrate surface. All samples except the sample of isolated quantum dots underwent a cleaning procedure based on acetone before SILAR was performed on them that might not be suitable for that purpose. The sample of isolated quantum dots, used as received, did not undergo such a cleaning procedure but yielded more desirable results. To reliable achieve quantum dot nucleation on rutile (100) the necessity for proper cleaning must be investigated. For example Jang *et al.* use a more rigorous cleaning procedure in their rutile centered experiments.[28] Another indication for the importance of proper cleaning is, that many samples with dirty surfaces look similar to the polycrystalline lead sulfide samples obtained by Kanniainen *et al.*, see Figure 9a on page 11 for an example.[14] Those thin films were grown on amorphous glass as substrate. A rutile (100) surface covered by a layer of organic dirt can be considered to be rather amorphous on its surface. Therefore all the assumptions about lattice mismatch and strain induced island formation would be obsolete and random nucleation would take place leading to dense polycrystalline coatings with lead sulfide.

However, the synthesized quantum dots of the sample of isolated quantum dots share many properties with quantum dots from classical epitaxial growth methods. A direct comparison of atomic force microscope images of the SILAR made quantum dots and a sample from molecular beam epitaxy is shown in Figure 31.

A homogeneous distribution of quantum dots is assumed for the sample of isolated quantum dots. The areal number density of the sample of isolated quantum dots is about four times lower than the one of the sample in Figure 31b.[30] To increase the density one could do follow up experiments based on the current work of Lee *et al.* who used triethanolamine to increase the areal number density of quantum dots on mesoporous titanium dioxide.[32] Triethanolamine as complexing agent was already used 1996 by Kanniainen *et al.* to increase the lead sulfide growth rate per SILAR cycle in thin film experiments. This work of Kanniainen *et al.* was already cited in the context of the cycle dependent experiments presented in section 3, page 48.[27]

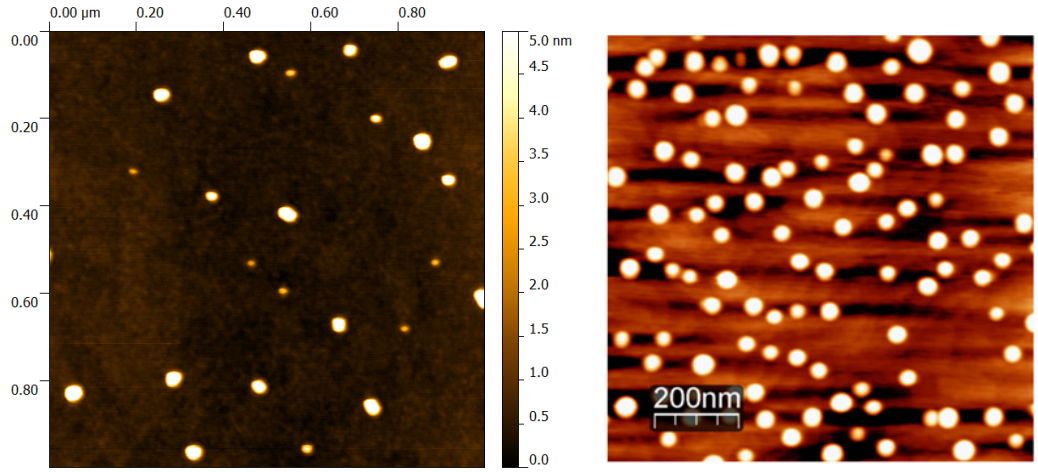

(a) AFM: PbS QDs, 2 cycles SILAR (b) AFM: InAs/GaAs QDs, MBE [30]

Figure 31.: Comparison of quantum dot topography

Aspect Ratio

An aspect ratio of 0.16 ± 0.08 was found for the quantum dots in the sample of isolated quantum dots in subsection 2.4.4, page 34. The aspect ratio distribution was found to have one peak, whereas the height and diameter distributions of the quantum dots were bimodal. Having two types of quantum dots is another feature mimicking epitaxial growth. In the calculated phase diagram for epitaxial growth mechanisms shown in Figure 7 on page 9 the predicted phases R_2 and R_3 are models for this bimodal behavior. For epitaxial indium phosphide (InP) quantum dots grown by metal-organic vapor-phase epitaxy (MOVPE) Schulz *et al.* found a bimodal distribution of height and diameter, while the aspect ratio was not bimodal distributed.[33]

While a bimodal distribution could be of interest for light emitting diodes that emit two colors at the same time, or solar cells harvesting light of two different wavelengths, a narrow size distribution is preferred for most other use cases like lasers. Especially as there is currently no control on the size distribution more work is necessary on studying the nucleation to develop a mechanism that hopefully can predict the size distribution in the future.

As their height is found to be well below the lead sulfide exciton Bohr radius quantum confinement is expected. To proof this further studies like photoluminescence or cathodoluminescence are necessary.

Quantum Rods

This could be the first report of lead sulfide quantum rods obtained by SILAR. As of October 4, 2013 no publication could be found mentioning such a result like it

was presented in section 2.5, page 37. As an unexpected result this gave rise to new questions. Quantum rods evolved simultaneously with the quantum dots on the same substrate, so, how can one or the other be obtained without the respective counterpart? What is their growth mechanism? Where do they nucleate?

From subsection 2.5.2, page 40 the possibility was derived that rod growth might be induced by quantum dots, as rods often have smaller bulges at one of their ends. Rod length, height and width has a large variance, but rods are homogeneously distributed over the complete sampled area. Rods were found after two cycles SILAR, but their height is exceeding by a large amount the height of material predicted to be deposited after two cycles SILAR. Therefore the rod growth mechanism should differ from the quantum dot growth mechanism for SILAR. Perhaps the adsorption mechanism for precursor adsorption is different or material might be moved during the rinsing steps. However most rod should not show quantum confinement effects, as their smallest dimension is larger than exciton Bohr radius in lead sulfide.

subsection 2.5.1, page 37, confirmed the elemental composition to be lead and/or sulfur for the quantum rods. As for the quantum dot case as wetting layer can suspected to be found around the quantum rods.

If one want to continue studies on the lead sulfide quantum rods the main question to answer should be: What nucleates a rod? Possible answers that could be investigated in further experiments include: Dirt particles nucleate rods. Scratches and trenches, for example seen in Figure 13b, page 24 are seeds for rod nucleation. Terrace steps and dislocation in the surface might start rod nucleation. Perhaps a special sort of strain from lattice mismatch or other strain induces rod growth. Certain crystal facets of quantum dots grow faster than others, this will start preferential growth.[24]

Currently the appearance of quantum rods lacks explanation nearly completely. To answer the newly raised questions about rod evolution many of the afore mentioned things probably need to be thoroughly investigated.

Spectroscopic Attempts

UV-Vis and Fluorescence as presented in subsection 2.6.1, page 42 and subsection 2.6.2, page 44 were not able to verify quantum confinement. Therefore did not give proof of successful quantum dot synthesis. To prove the synthesis of quantum dots other methods like attenuated total reflectance and cathodoluminescence should be employed on the sample of isolated quantum dots to verify the synthesis of quantum dots.

On a sample with unknown topography scanning tunneling spectroscopy did not gave reproducible results in subsection 2.6.3, page 45. Scanning tunneling spectroscopy itself might be able to resolve effects caused by quantum confinement. Therefore this method should be employed on the sample of isolated quantum dots.

Appendix A.

Synthetic Procedures

A.1. SILAR PbS Quantum Dot Synthesis

$$Pb^{2+} \xrightarrow{TiO_2} Pb^{2+}(ads) \tag{A.1}$$

$$Pb^{2+}(ads) + S^{2-} \longrightarrow PbS(surf) \tag{A.2}$$

Table A.1.: Solutions for a SILAR synthesis

Substance	Molar mass	Amount		Solvent	Concentration
$Pb(NO_3)_2$	[331.21]	405 mg	1.2 mmol	60 mL Methanol	0.02 mol/L
Methanol I	[32.04]	60 mL			
Na_2S	[78.05]	95 mg	1.2 mmol	60 mL Methanol	0.02 mol/L
Methanol II	[32.04]	60 mL			
Methanol III	[32.04]	60 mL			

For SILAR lead sulfide quantum dot synthesis chemicals were used as received without further purification. Chromatography grade methanol (CH_3OH) was obtained from VWR. Lead nitrate ($Pb(NO_3)_2$) 99 % was obtained from Sigma-Aldrich. Sodium sulfide (Na_2S) 98 % was also obtained from Sigma-Aldrich

First, dissolved gaseous oxygen was removed from a total of 300 mL methanol. Two 250 mL round bottom flasks were filled with 150 mL methanol chromatography grade each and a stream of argon was bubbled through them for one hour. For that, each flask was equipped with a rubber septum, a long needle piercing the rubber septum immersing its end into the solution. The long needle was connected with silicone tubings to the argon part of a Schlenk line. As an exhaust for the flushed argon, a shorter needle was used to pierce the septum, inserting it only enough to go through the septum, but not reaching the surface of the liquid.

In a 100 mL screw cap bottle, 405 mg of lead nitrate was dissolved in 60 mL oxygen free methanol[1] by 45 min sonication to give a clear solution. In a second 100 mL screw

[1] "Oxygen free" refers to having as less oxygen (O_2(gas)) dissolved in the solution as possible, not removing oxygen atoms (O) from the methanol molecules (CH_3OH).

cap bottle 95 mg anhydrous sodium sulfide was dissolved in 60 mL methanol by 45 min sonication to give a white opaque solution. The remaining 180 mL of oxygen free methanol was divided into three 60 mL portions in 100 mL screw cap bottles labeled "methanol I", "methanol II" and "methanol III". All five bottles were transferred into a nitrogen atmosphere glove box.

Under inert atmosphere the substrate[2] was immersed into 60 mL methanol III for thirty seconds before the SILAR cycles were performed. One cycle consisted of 20 s immersion into 0.02 mol/L methanolic $Pb(NO_3)_2$ solution, 30 s immersion into methanol I rinsing bath, 20 s immersion into 0.02 mol/L methanolic Na_2S solution and 30 s immersion into methanol II rinsing bath. As the rinsing baths I and II might get polluted over the increasing number of SILAR cycles, a final 50 s immersion into 60 mL of methanol III was carried out after the completed SILAR process. A summary of the immersion times during a SILAR process is available in Table A.2 The sample was allowed to dry in inert atmosphere. For batch processing multiple samples another 60 mL of oxygen free methanol were used as wetting bath before the SILAR cycles instead of using the final rinsing bath methanol III.

Table A.2.: Immersion times for a SILAR process with n cycles

Step	No. of immersions	Immersion time / s
Wetting	1	30
Pb^{2+}	n	20
Rinse I	n	30
S^{2-}	n	20
Rinse II	n	30
Rinse III	1	50

A.1.1 Partial Sample Exposure to SILAR

To increase the number of experiments performed on a sample, it can be partly covered with parafilm. The common sample size is 10 mm by 5 mm with a thickness of 0.5 mm. The area of 10 mm by 5 mm can easily be divided into five strips of 2 mm by 5 mm. Those 2 mm long strips are big enough to unambiguously identify them with the help of a simple millimeter scale ruler. Further they are large enough to provide multiple spots to measure AFM and SEM. To cover four fifths of the sample cut out a piece of parafilm, approximately 13 mm by 9 mm. For covering three out of five parts of a normal substrate a 13 mm by 7 mm patch of parafilm should be cut out, and so on. The parafilm is now wrapped around the substrate using two pairs of tweezers. Figure A.1a shows how the parafilm extends from the substrate a bit to the right. In the top views (Figure A.1b and A.1c) the parafilm extends away from the substrate a bit from the

[2]Here mostly a titanium dioxide crystal of the rutile phase with polished (100) and (-100) faces.

upper part in the image. Some pressure, for example applied with a spatula, makes the parafilm less likely to detach itself from the substrate. The substrate is now held by a tweezer at the uncovered part and sealing is finalized by heating for a few seconds with a hot air gun. After the SILAR process the parafilm can be pulled off with two pairs

(a) Side view (b) Top view part 1 (c) Top view part 2

Figure A.1.: Wrapping a substrate in parafilm, dimensions are not to scale

of tweezers. Some parafilm residue will remain on the previously covered parts of the sample. This residue needs to be thoroughly removed before further experiments are performed. A combination of scrubbing with alcohol or acetone soaked cotton swabs, sonicating at 40 °C in acetone or alcohol for 15 min, with a final rinse of clean solvent were usually done.

Appendix B.

Analytical methods

B.1. Atomic Force Microscopy

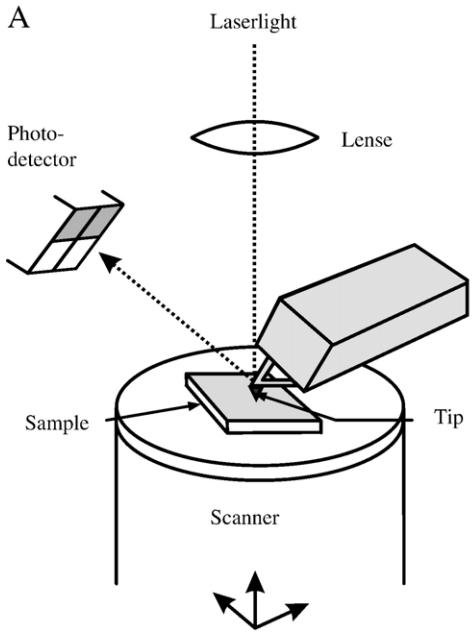

Figure B.1.: Basic working principle of atomic force microscopy [41]

Atomic force microscopy (AFM) belongs to the class of scanning probe microscopes (SPM),[42] a sample is scanned, or rasterized, by moving its surface under the tip of a cantilever. As seen in Figure B.1 a laser beam is focused on the cantilever tip from where it is reflected to a photo-detector that can spatially resolve where it is hit by the laser beam. A cantilever bending towards the sample will reflect the laser light to a different position than a cantilever at rest, or one bending away from the sample. As long as there are attractive or repulsive forces between the sample surface and the cantilever tip, the response of the photo-detector is a measure of these forces. Most commonly these forces are approximated with a Lenard-Jones potential taking into account only attractive van-der-Waals forces, Coloumb interaction and Pauli repulsion.

$$V(r) = \frac{A}{r^{12}} - \frac{B}{r^6} \tag{B.1}$$

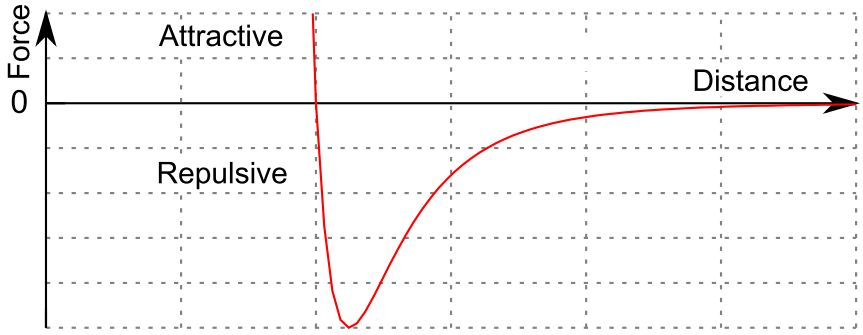

Figure B.2.: Lenard-Jones potential

In Equation B.1 the Lenard-Jones potential $V(r)$ is a function of two constants A, B and the distance r between sample and cantilever tip. Pauli repulsion is modeled together with the also repulsive Coulomb interaction to go with distance to the power of 12, whereas van-der-Waals forces are modeled to go with distance to the power of six. An arbitrary sample of how a Lenard-Jones potential looks is depicted in Figure B.2. This approximation is valid for distances smaller than 5 nm. For larger distances other interactions such as electrostatic or capillary forces play a more important role. Unfortunately they depend less on the actual surface topography, which is of main interest for this research.

The scanner usually is carried out as a tubular piezoeletric element. Piezos can be deformed by applying a voltage across them. This is used to move the sample in three dimensions. An aspect to highlight is that for most piezoeletric materials, like lead titanate zirconate ($PbTiO_3 + PbZrO_3$), there is a linear relation between applied voltage and deformation. This yields a theoretical infinite high resolution in the movement. Furthermore the response time is in the range microseconds, so they are fast enough to scan a certain area in finite time. One downside is the often encountered hysteresis from polarization in the piezoelectric material, but this can be dealt within a closed feedback loop.

The operational modes of atomic force microscopes are divided into two classes, static modes and dynamic modes. In dynamic modes the cantilever is excited to oscillate, in static modes the cantilever is not excited. The two most common static modes are closely connected to Hooke's law, Equation B.2.

$$F = -k \cdot z \tag{B.2}$$

Here F is the force applied to the cantilever tip, k the spring constant of the cantilever, and z the deflection of the cantilever. An atomic force microscope in constant height mode scans the sample with the cantilever at a fixed distance z away from the sample.

The deflection of the cantilever provides a measure of the sample's topography and other interactions with the tip. In constant force mode the force F is set by the experimentalist. While scanning in x and y directions a feedback loop varies the distance z to keep the force constant. The extension of the piezo z is read out as the signal of the sample's topography.

In dynamic modes the amplitude and frequency of the cantilever oscillation are observed. For the frequency modulated variant the cantilever is excited to its resonant frequency. Tip sample interactions now change the oscillating frequency. In amplitude modulated mode, also called tapping mode, the cantilever is excited to an amplitude set point while the frequency is kept constant. The amplitude deviation induced by tip sample interaction is then recorded as topographic signal. As the tip is not in permanent contact with the sample, less force is applied to the surface and even weakly adsorbed species can be mapped on a surface. In static modes those weakly adsorbed species, like polymers or proteins, often are absorbed to the tip itself and dragged around on the surface. Overall tapping mode is a very robust method to routinely investigate samples with unknown characteristics.

B.1.1 AFM Equipment, Measurements and Data Processing

For atomic force microscopy (AFM), either a Bruker MultiMode equipped with a NanoScope 3a controller or a Bruker MultiMode equipped with a NanoScope 5 controller was operated in tapping mode. Cantilevers were type OMCL-AC160TS from Olympus. They are made of silicon with an aluminum reflective coating, have a resonance frequency of (300 ± 100) kHz and a typical tip radius of 7 nm.

Samples were glued to magnetic discs before mounted in the atomic force microscope. After the measurements samples were routinely removed from the magnetic disc by sonicating them for 15 min in 40 °C technical grade acetone. Subsequently macroscopic remains of glue were removed with acetone soaked cotton swabs. Again the sample were sonicated for 15 min in 40 °C technical grade acetone and rinsed with ambient temperature acetone before they were rinsed with fresh acetone.

Typically, areas of 1 µm by 1 µm were scanned with a resolution of 512 pixels by 512 pixels. Scan frequency varied between 0.2 Hz and 2 Hz.

With the `Gwyddion` computer software, the following steps were routinely performed to process the raw AFM data: First, a mask was applied to exclude features outlying in height, like quantum dots and other grains, from all further averaging. Second, the mean height was subtracted from each pixel. Third, the mask was adjusted for features that were not apparent from the beginning. Fourth, neighboring lines were corrected to match the height median of their respective neighbors. Finally, the minimum height value was set to zero.

For scan areas 5 µm by 5 µm and larger, polynomial background removal was performed with polynomial degrees up to 4 in vertical and horizontal directions to correct for scanner bow, if needed.

B.2. Scanning Electron Microscope & Energy Dispersive X-Ray Spectroscopy

Scanning electron microscopy and energy dispersive X-ray spectroscopy was performed on a Hitachi SU8000 Ultra-High-Resolution FE-SEM system. The device was operated by Gunnar Glaßer.

An introduction into the powerful method of hyper maps and elemental maps obtainable from energy Dispersive X-ray spectroscopy is available in reference [29].

Appendix C.

Computer Software

C.1. Gwyddion

An overview about `Gwyddion` is given in reference [43]. For atomic force microscope data analysis `Gwyddion` version 2.30 was used. `Gwyddion` is a piece of free, open source software, distributed under the GNU General Public License and can be obtained from `http://gwyddion.net`.

To automatically calculate the heights of an ensemble of quantum dots marked with a *mask* in `Gwyddion` a user defined *grain analysis function* was added following a suggestion from the "Gwyddion user guide".[44] According to that the code contained in Listing C.1 was saved as a text file `grainheigt.txt` in the appropriate folder on the computer running `Gwyddion`. For the operation system `Windows 7` in its English localization this path was `C:\Users\USERNAME\gwyddion\grainvalues`, for most `Linux` and `Unix` operation systems `/home/USERNAME/.gwyddion/grainvalues` or its short handle `~/.gwyddion/grainvalues` would be appropriate.

Listing C.1: Implementation of *Grain height* calculation

```
Gwyddion resource GwyGrainValue
symbol dz
symbol_markup Δz
power_xy 0
power_z 1
expression z_max − z_min
```

C.2. Gnuplot

Graphs were plotted using `gnuplot` in version 4.6 patchlevel 0 last modified 2012-03-04 for MS-Windows 32 bit. `gnuplot` is free, open source software distributed under its own license and can be downloaded from `http://www.gnuplot.info`.

Bibliography

[1] S. Emin, S. P. Singh, L. Han, N. Satoh, A. Islam, "Colloidal quantum dot solar cells," *Solar Energy* **2011**, *85*, 1264–1282, DOI 10.1016/j.solener.2011.02.005 (cit. on p. 4).

[2] J. Olson, G. Gray, S. Carter, "Optimizing hybrid photovoltaics through annealing and ligand choice," *Solar Energy Materials and Solar Cells* **2009**, *93*, 519–523, DOI 10.1016/j.solmat.2008.11.022 (cit. on p. 4).

[3] P. Kamat, Solar Cells, **Oct. 2013**, http://www3.nd.edu/~kamatlab/research_solarCells.html (visited on 10/04/2013) (cit. on p. 4).

[4] F. Maier-Flaig, J. Rinck, M. Stephan, T. Bocksrocker, M. Bruns, C. Kübel, A. K. Powell, G. A. Ozin, U. Lemmer, "Multicolor Silicon Light-Emitting Diodes (SiLEDs)," *Nano Lett.* **2013**, *13*, 475–480, DOI 10.1021/nl3038689 (cit. on p. 5).

[5] H. Pathan, C. Lokhande, "Deposition of metal chalcogenide thin films by successive ionic layer adsorption and reaction (SILAR) method," *Bulletin of Materials Science* **2004**, *27*, 85–111, DOI 10.1007/BF02708491 (cit. on pp. 6, 9, 10, 16).

[6] H. Lan, Y. Ding, "Ordering, positioning and uniformity of quantum dot arrays," *Nano Today* **2012**, *7*, 94–123, DOI 10.1016/j.nantod.2012.02.006 (cit. on p. 6).

[7] Universidad Politécnica de Madrid, Instituto de Sistemas Optoelectrónicos y Microtecnología, http://www.isom.upm.es/equipos/MBE.php (cit. on p. 7).

[8] D. Bimberg, M. Grundmann, N. N. Ledencov, *Quantum dot heterostructures*, Wiley, Chichester, 1st ed., **1999**, ISBN: 0-471-97388-2 (cit. on p. 6).

[9] I. Daruka, A.-L. Barabási, "Dislocation-Free Island Formation in Heteroepitaxial Growth: A Study at Equilibrium," *Physical Review Letters* **Nov. 1997**, *79*, 3708–3711, DOI 10.1103/PhysRevLett.79.3708 (cit. on pp. 8, 9, 36, 49).

[10] M. Brehm, F. Montalenti, M. Grydlik, G. Vastola, H. Lichtenberger, N. Hrauda, M. J. Beck, T. Fromherz, F. Schäffler, L. Miglio, G. Bauer, "Key role of the wetting layer in revealing the hidden path of Ge/Si(001) Stranski-Krastanow growth onset," *Physical Review B* **Nov. 2009**, *80*, 205321, DOI 10.1103/PhysRevB.80.205321 (cit. on p. 8).

[11] O. Moutanabbir, S. Miyamoto, E. E. Haller, K. M. Itoh, "Transport of Deposited Atoms throughout Strain-Mediated Self-Assembly," *Physical Review Letters* **July 2010**, *105*, 026101, DOI 10.1103/PhysRevLett.105.026101 (cit. on p. 8).

[12] O. Schmidt, *Lateral Aligment of Epitaxial Quantum Dots*, Springer, Berlin, Heidelberg, **2007**, DOI 10.1007/978-3-540-46936-0 (cit. on pp. 8, 34).

[13] Y. Nicolau, "Solution deposition of thin solid compound films by a successive ionic-layer adsorption and reaction process," *Applications of Surface Science* **1985**, *22–23, Part 2*, 1061–1074, DOI http://dx.doi.org/10.1016/0378-5963(85)90241-7 (cit. on p. 9).

[14] T. Kanniainen, S. Lindroos, R. Resch, M. Leskelä, G. Friedbacher, M. Grasserbauer, "Structural and topographical studies of SILAR-grown highly oriented PbS thin films," *Materials Research Bulletin* **2000**, *35*, 1045–1051, DOI http://dx.doi.org/10.1016/S0025-5408(00)00298-1 (cit. on pp. 11, 19, 20, 50).

[15] H. Lee, M. Wang, P. Chen, D. R. Gamelin, S. M. Zakeeruddin, M. Grätzel, M. K. Nazeeruddin, "Efficient CdSe Quantum Dot-Sensitized Solar Cells Prepared by an Improved Successive Ionic Layer Adsorption and Reaction Process," *Nano Letters* **Dec. 2009**, *9*, 4221–4227, DOI 10.1021/nl902438d (cit. on pp. 10, 11).

[16] N. Guijarro, T. Lana-Villarreal, T. Lutz, S. A. Haque, R. Gómez, "Sensitization of TiO2 with PbSe Quantum Dots by SILAR: How Mercaptophenol Improves Charge Separation," *The Journal of Physical Chemistry Letters* **2012**, *3*, 3367–3372, DOI 10.1021/jz301528a (cit. on p. 10).

[17] H. Lee, H. C. Leventis, S.-J. Moon, P. Chen, S. Ito, S. A. Haque, T. Torres, F. Nüesch, T. Geiger, S. M. Zakeeruddin, M. Grätzel, M. K. Nazeeruddin, "PbS and CdS Quantum Dot-Sensitized Solid-State Solar Cells: "Old Concepts, New Results"," *Advanced Functional Materials* **2009**, *19*, 2735–2742, DOI 10.1002/adfm.200900081 (cit. on p. 10).

[18] U. Diebold, "The surface science of titanium dioxide," *Surface Science Reports* **2003**, *48*, 53–229, DOI 10.1016/S0167-5729(02)00100-0 (cit. on p. 11).

[19] I. Langmuir, "The Constitution and Fundamental Properties of Solids and Liquids. Part I. Solids.," *Journal of the American Chemical Society* **1916**, *38*, 2221–2295, DOI 10.1021/ja02268a002 (cit. on p. 11).

[20] P. W. Atkins, J. De Paula, *Atkins Physical Chemistry*, Oxford Univ. Press, Oxford, 7th ed., **2002** (cit. on p. 11).

[21] A. Braga, S. Giménez, I. Concina, A. Vomiero, I. Mora-Seró, "Panchromatic Sensitized Solar Cells Based on Metal Sulfide Quantum Dots Grown Directly on Nanostructured TiO_2 Electrodes," *The Journal of Physical Chemistry Letters* **2011**, *2*, 454–460, DOI 10.1021/jz2000112 (cit. on p. 12).

[22] L. J. Hillenbrand, "Reaction of PbS Surfaces with Oxygen," *The Journal of Chemical Physics* **1964**, *41*, 3971–3977, DOI 10.1063/1.1725844 (cit. on p. 13).

[23] *CRC Handbook of Chemistry and Physics, Vol. 94*, (Eds.: W. M. Haynes, D. R. Lide), CRC Press, Boca Raton, **2013**, 2668 pp., http://www.hbcpnetbase.com (cit. on pp. 13, 16).

[24] D. Kim, D.-H. Kim, J.-H. Lee, J. C. Grossman, "Impact of Stoichiometry on the Electronic Structure of PbS Quantum Dots," *Physical Review Letters* **May 2013**, *110*, 196802, DOI 10.1103/PhysRevLett.110.196802 (cit. on pp. 16, 52).

[25] E. Riedel, *Anorganische Chemie*, de Gruyter, Berlin, 5. Aufl., **2002**, ISBN: 3-11-017439-1 (cit. on p. 16).

[26] Y. Noda, K. Masumoto, S. Ohba, Y. Saito, K. Toriumi, Y. Iwata, I. Shibuya, "Temperature dependence of atomic thermal parameters of lead chalcogenides, PbS, PbSe and PbTe," *Acta Crystallographica Section C* **Aug. 1987**, *43*, 1443–1445, DOI 10.1107/S0108270187091509 (cit. on p. 16).

[27] T. Kanniainen, S. Lindroos, J. Ihanus, M. Leskela, "Growth of strongly orientated lead sulfide thin films by successive ionic layer adsorption and reaction (SILAR) technique," *Journal of Materials Chemistry* **1996**, *6*, 161–164, DOI 10.1039/JM9960600161 (cit. on pp. 22, 48, 50).

[28] J. H. Jang, F. Lydiatt, R. Lindsay, S. Baldelli, "Quantitative Orientation Analysis by Sum Frequency Generation in the Presence of Near-Resonant Background Signal: Acetonitrile on Rutile TiO2 (110)," *The Journal of Physical Chemistry A* **2013**, *117*, 6288–6302, DOI 10.1021/jp401019p (cit. on pp. 27, 50).

[29] T. Salge, R. Terborg, "EDS Microanalysis with the Silicon Drift Detector (SDD): Innovative Analysis Options for Mineralogical and Material Science Applications," *Anadolu University Journal of Science and Technology* **2009**, *10*, http://btdarsiv.anadolu.edu.tr (cit. on pp. 31, 59).

[30] C. Schneider, S. Kremling, N. V. Tarakina, T. Braun, M. Adams, M. Lermer, S. Reitzenstein, L. Worschech, M. Kamp, S. Höfling, A. Forchel, "AlGaInAs quantum dot solar cells: tailoring quantum dots for intermediate band formation," *Semiconductor Science and Technology* **2012**, *27*, 032002, DOI 10.1088/0268-1242/27/3/032002 (cit. on pp. 34, 50, 51).

[31] L. Li, G. Patriarche, N. Chauvin, P. Ridha, M. Rossetti, J. Andrzejewski, G. Sek, J. Misiewicz, A. Fiore, "Controlling the aspect ratio of quantum dots: From columnar dots to quantum rods," *Selected Topics in Quantum Electronics IEEE Journal of* **2008**, *14*, 1204–1213, DOI 10.1109/JSTQE.2008.919719 (cit. on p. 34).

[32] J.-W. Lee, J.-D. Hong, N.-G. Park, "Sixfold enhancement of photocurrent by surface charge controlled high density quantum dot coating," *Chemical Communications* **2013**, *49*, 6448–6450, DOI 10.1039/C3CC42896F (cit. on pp. 34, 50).

[33] W.-M. Schulz, R. Roßbach, M. Reischle, G. J. Beirne, M. Bommer, M. Jetter, P. Michler, "Optical and structural properties of InP quantum dots embedded in $(Al_xGa_{1-x})_{0.51}In_{0.49}P$," *Physical Review B* **Jan. 2009**, *79*, 035329, DOI 10.1103/PhysRevB.79.035329 (cit. on pp. 36, 51).

[34] T. R. Ramachandran, R. Heitz, P. Chen, A. Madhukar, "Mass transfer in Stranski-Krastanow growth of InAs on GaAs," *Applied Physics Letters* **1997**, *70*, 640–642, DOI 10.1063/1.118848 (cit. on p. 36).

[35] I. Goldfarb, P. T. Hayden, J. H. G. Owen, G. A. D. Briggs, "Competing growth mechanisms of Ge/Si(001) coherent clusters," *Phys. Rev. B* **Oct. 1997**, *56*, 10459–10468, DOI 10.1103/PhysRevB.56.10459 (cit. on p. 36).

[36] D. C. Cronemeyer, "Electrical and Optical Properties of Rutile Single Crystals," *Physical Review* **Sept. 1952**, *87*, 876–886, DOI 10.1103/PhysRev.87.876 (cit. on pp. 42, 43, 46).

[37] E. Cánovas, A. Martí, A. Luque, C. D. Farmer, C. R. Stanley, A. M. Sánchez, T. Ben, S. I. Molina, "Lateral absorption measurements of InAs/GaAs quantum dots stacks: Potential as intermediate band material for high efficiency solar cells," *Energy Procedia* **2010**, *2*, 27–34, DOI http://dx.doi.org/10.1016/j.egypro.2010.07.006 (cit. on p. 42).

[38] Q. Kang, S. Liu, L. Yang, Q. Cai, C. A. Grimes, "Fabrication of PbS Nanoparticle-Sensitized TiO2 Nanotube Arrays and Their Photoelectrochemical Properties," *ACS APPLIED MATERIALS and INTERFACES* **Mar. 2011**, *3*, 746–749, DOI 10.1021/am101086t (cit. on p. 43).

[39] R. Brahimi, Y. Bessekhouad, A. Bouguelia, M. Trari, "Improvement of eosin visible light degradation using PbS-sensititized TiO2," *Journal of Photochemistry and Photobiology A: Chemistry* **2008**, *194*, 173–180, DOI http://dx.doi.org/10.1016/j.jphotochem.2007.08.008 (cit. on p. 43).

[40] A. Balzarotti, "The evolution of self-assembled InAs/GaAs(001) quantum dots grown by growth-interrupted molecular beam epitaxy," *Nanotechnology* **2008**, *19*, 505701 (cit. on p. 48).

[41] H.-J. Butt, R. Berger, E. Bonaccurso, Y. Chen, J. Wang, "Impact of atomic force microscopy on interface and colloid science," *Advances in Colloid and Interface Science* **2007**, *133*, 91–104, DOI 10.1016/j.cis.2007.06.001 (cit. on p. 56).

[42] G. Binnig, C. F. Quate, C. Gerber, "Atomic Force Microscope," *Physical Review Letters* **Mar. 1986**, *56*, 930–933, DOI 10.1103/PhysRevLett.56.930 (cit. on p. 56).

[43] D. Nečas, P. Klapetek, "Gwyddion: an open-source software for SPM data analysis," *Central European Journal of Physics* **2012**, *10*, 181–188, DOI 10.2478/s11534-011-0096-2 (cit. on p. 60).

[44] P. Klapetek, D. Nečas, C. Anderson, Gwyddion user guide, **Sept. 2013**, http://gwyddion.net/download/user-guide (visited on 09/30/2013) (cit. on p. 60).